Data driven modeling of junction flows

Geneviève Vigner

Supervisor

Dr. Richard Dwight
Associate Professor
Aerodynamics research group
TU Delft

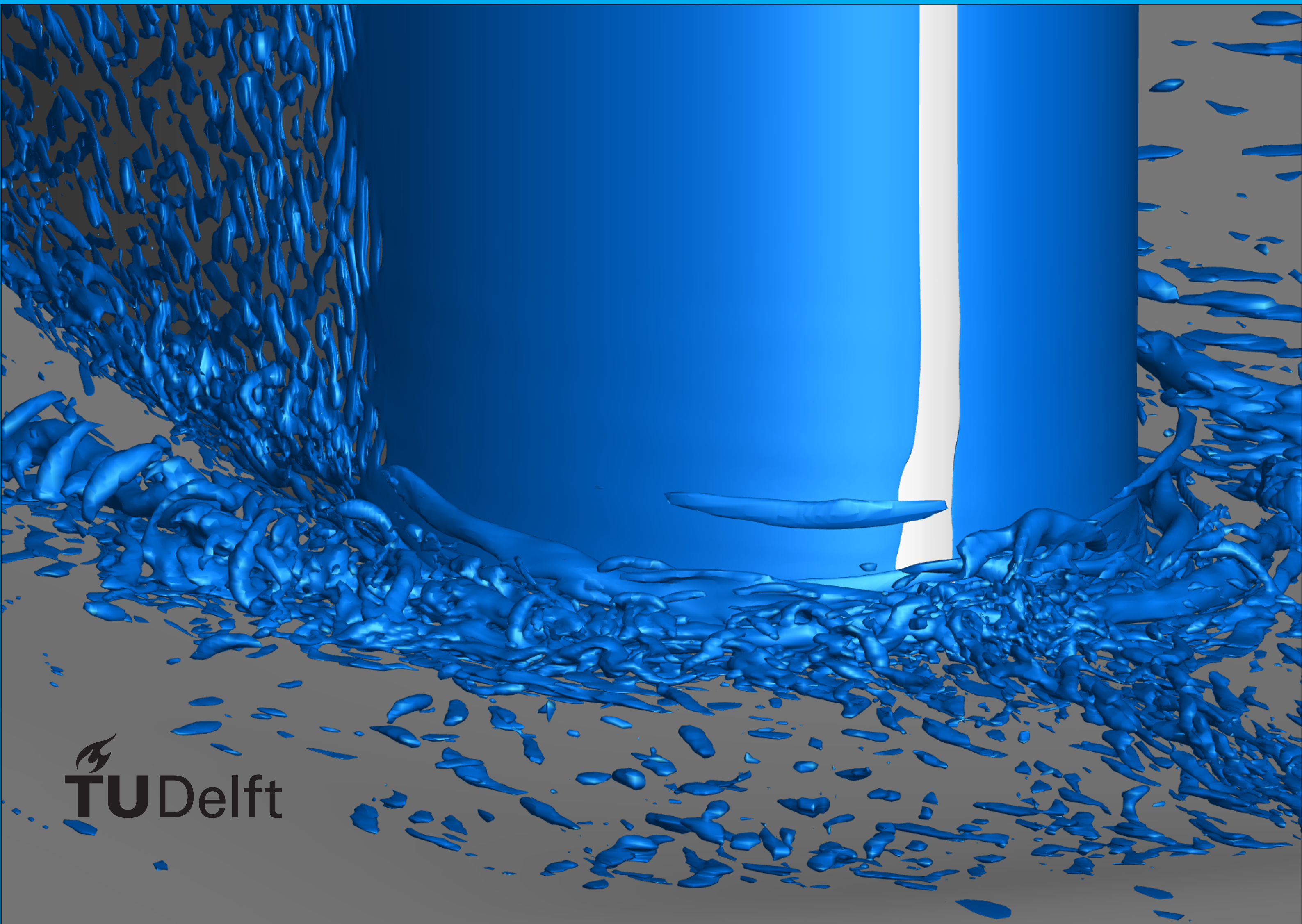

Data driven modeling of junction flows

by

Geneviève Vigner

to obtain the degree of Master of Science
at the Delft University of Technology,
to be defended publicly on Tuesday February 25, 2022 at 9:30 AM.

Student number:	5150825	
Project duration:	March 8, 2021 – February 25 , 2022	
Thesis committee:	Dr. R.P. Dwight,	TU Delft, supervisor
	Prof. Dr. Ing. G. Eitelberg ,	TU Delft
	Dr. S. J. Hulshoff ,	TU Delft

An electronic version of this thesis is available at `http://repository.tudelft.nl/`.

Acknowledgements

This thesis was conducted as part of the master in Aerospace Engineering at the Delft University of Technology.

First, I would like to thank my supervisor Dr. Richard Dwight for giving me the opportunity to work on this subject and for his feedbacks and discussions along the project. Many thanks also to Jasper Alberts, who initially started on this project, for always being present to answer my questions during the thesis. Thanks also to Dr. Steven Hulshoff for his help when dealing with the M16 servers.

Finally, I would like to thank my parents and my boyfriend for their constant support during this thesis and along my studies at TU Delft.

Geneviève Vigner
Paris, February 2022

Abstract

A wall resolved LES simulation of the Anti-Fairing wing/body junction introduced by Belligoli et al. [6] to reduce interference drag is performed. The LES mesh is composed of 61.7 million cells with a C-fitted grid around the wing . The simulation is performed using the pimple solver of OpenFoam 4 with a time and space varying inlet boundary condition obtained thanks to a precursor. This simulation will be used to assess the impact of the Anti-Fairing by comparing the result to the wall resolved baseline case of Alberts [2] and to serve as a training data for data driven techniques applied to junctions flows.

Using the wall resolved LES we apply the data driven algorithm method Sparse Regression of Turbulent Stress Anisotropy (SpaRTA) developed by Schmelzer et al. [38] in the case of junction flows. It is shown that the first step of the method, namely the k-corrective frozen RANS, is able to produce corrective fields to the Reynolds tensor and the turbulent kinetic energy equations in this case. The corrective fields once added in a $k-\omega\ SST$ simulation make it possible to obtain the exact location, strength and shape of the main horseshoe vortex. The upstream boundary layer is also subject to corrections indicating RANS-LES mismatch in the inflow. Mutual Information (MI) is calculated to identify the relevant tensors, physical features and invariants that correlate with the junction flow data. Finally, algebraic models for the corrective fields are obtained. They are compared to the true values of these fields. It is possible to see that the performance of SpARTA models is good upstream of the wing. However, models found and tested in the vicinity of the wing, where the separation and horseshoe vortex are located, are not fully able to capture the relevant corrections. Additional constraints or steps to the ones performed in the time of this study may be necessary in order to use SpaRTA to generate models giving improved predictions compared to classic RANS turbulence models.

Contents

Nomenclature

Abbreviations

BF	Bluntness factor
c	Chord lenght
CFL	Courant–Friedrichs–Lewy
DES	Detached Eddy Simulation
DIC	Diagonal Incomplete-Cholesky
DMD	Dynamic Mode Decomposition
DNS	Direct Numerical Simulation
FI	Field Inversion
GEP	Genetic expression programming
HV	Horseshoe Vortex
LES	Large Eddy Simulation
MDF	Momentum Deficit Factor
MI	Mutual Information
NN	Neural Networks
PCG	Preconditioned Conjugate Gradient
PDF	Probability density function
POD	Proper Orthogonal Decomposition
PV	Primary Vortex
$RANS$	Reynolds Averaged Navier Stokes
RF	Random Forests
SGS	Subgrid scale
$SpaRTA$	Sparse Regression of Turbulent Stress Anisotropy
SV	Secondary Vortex
$t.k.e$	turbulent kinetic energy
TCF	Turbulent channel flow

Greek Letters

β	Training data
Δt	Timestep
Δx	Cell size
δ^*	Displacement thickness
η	Ensemble of Features
λ_n	Invariants
ν	Molecular viscosity
ν_t	Turbulent viscosity
Ω	Mean rotation rate
ω	Specific dissipation rate
$\Omega_{x,y,z}$	Components of the vorticity
ρ	Density
τ_{ij}	Reynolds stress
θ	Boundary layer momentum thickness
$\widetilde{\Omega}$	Normalized Mean rotation rate

Latin Letters

$\widetilde{S}$	Normalized Mean strain rate
B	Library
b_p	Turbulent channel flow width
b_{ij}^0	Boussinesq Anisotropic Reynolds stress
b_{ij}^Δ	Anisotropic Reynolds stress correction
C	Library
c	Chord length
C_p	Pressure coefficient
H	Entropy
h_p	Turbulent channel flow height
k	turbulent kinetic energy
l_p	Turbulent channel flow length
P	Pressure
P_∞	Freestream pressure
P_k	Production of turbulent kinetic energy
P_k^0	Boussinesq production of turbulent kinetic energy
q	Physical features
R	Turbulent kinetic energy deficit
R_0	Leading edge radius
Re_θ	Reynolds number associated the boundary layer thickness
S	Mean strain rate
S_T	Distance between the leading edge and the maximum thickness
T	Maximum thickness of the wing
t	Time
$T^{(n)}$	Tensors basis
U	Streamwise velocity
U_∞	Freestream velocity
U_b	Bulk velocity
U_{ref}	Freestream velocity
V	Normal to the wall velocity
X	Streamwise spacial component
X_T	Chordwise position of the maximum thickness
Y	Normal to the wall spacial component
y^+	Non-DimensionalWall Distance
Z	Spanwise component

List of Figures

1

Introduction

Junction flows are encountered when a boundary layer developed on a surface meets an obstacle attached to it (Simpson [41]). This specific configuration leads to the separation of the boundary layer upstream of the obstacle. In addition, the flow generally presents a system of unsteady vortices and a corner separation. The appearance and strength of these two characteristics depend, among other factors, on the design of the junction (Fleming et al. [13],Belligoli et al. [6]), the thickness of the incoming boundary layer (Fleming et al. [14]) as well as the angle of attack and swept of the wing in case of a body wing junction (Simpson [41]). Junction flows present some adverse effects such as pressure and heat transfer fluctuations as well as interference drag. The solutions have generally concentrated on reducing the size of the vortices by adding suction of the incoming boundary layer or by adding a fillet at the leading edge or around the wing. Aerodynamic shape optimization has been employed by Belligoli et al. [6] to reduce the interference drag, leading to a novel design of the junction called the Anti-Fairing.

Direct Numerical Simulation (DNS) of the Navier-Stokes equations is not possible in most cases due to the high computational cost of their resolution. Large Eddy Simulation (LES) constitutes the second most accurate technique, modeling only the influence of the smallest scales of the flow on the bigger scales. Ryu et al. [37] performed an LES simulation of the body wing junction, reaching an excellent agreement with the previous experiments. However, these types of simulations are also too expensive to be used in applications such as design. Reynolds Averaged Navier Stokes (RANS), due to its low computational cost remains today the main tool for industry purposes. However, numerous studies (Apsley and Leschziner [3], Lee et al. [24], Paciorri et al. [32] ,Gand et al. [15]) demonstrated the lack of accuracy of RANS predictions for body wing junctions. The location, strength, and size of the time-mean vortex are not properly captured. Unphysical behavior for the turbulent kinetic energy is also predicted in some types of RANS models. The poor performance of these affordable models makes it necessary to develop new methodologies with low computational cost to improve the body wing junctions predictions.

In recent years, machine learning applied to fluid dynamics has gained interest, and data-driven techniques have been tested on different types of flows (Duraisamy et al. [12]). In particular, the Sparse Regression of Turbulent Stress Anisotropy (SpaRTA) approach developed by Schmelzer et al. [38] has provided good results in the case of 2D flows, bluff bodies (Huijing et al. [17]) and wind turbine wakes (Steiner et al. [44]). Yet, the SpaRTA has not been tested for the modeling of body wing junctions. As a consequence, this project will aim at generating a wall resolved LES of the Anti-Fairing body wing junction and at testing the capability of the SpaRTA methodology at generating improved RANS models for this specific case.

A literature review on junction flows and machine learning for augmentation of RANS models is performed in section 2. Then Section 3 presents the methodology that will be followed for the project. Section 4 contains the results of the LES of the Anti-Fairing body wing junction and its comparison with the baseline case. Section 5 shows the results of the SpaRTA methodology and Section 6 concludes and presents some recommendations for future works.

2

Literature study

In this chapter, the relevant background to the study is presented. First, the notion of junction flow is presented. The characteristics that can be observed in these types of flow are detailed as well as the parameters that can influence these characteristics. A sum-up of the numerical attempts to model body wing junctions is also shown to understand how machine learning techniques can be of interest in the modeling of such flows. The section on junction flows concludes with the detrimental effects caused by the junction and which techniques have been employed to mitigate them. Of specific interest is the Anti-Fairing design of the junction as a wall resolved LES of it will be performed by the author.

The presentation of previously used numerical modeling highlights the need for new techniques to have an accurate representation of junction flows. In this work, the use of machine learning techniques has been chosen. The second section of this introduction constitutes a presentation on machine learning applied to fluid mechanics. The important steps in generating data-driven models are listed as well as the techniques used by various authors at each of these steps. Among these techniques, the one retained in this work is the Sparse Regression of Turbulent Stress Anisotropy (SparTA) technique, it will be discussed in more details in Section 3.2.

2.1. Junction flows

Junction flows appear when the boundary layer developed on a wall meets an obstacle connected to this wall. They are encountered in many situations such as turbine blades, river bridges, or wing body junctions in the case of an airplane.

2.1.1. Characteristic features of junction flows

Junction flows present two main types of features: the first one is a system of horseshoe vortices, and the second is a corner separation at the trailing edge. The strength and appearance of these two features are still subject to questions. Due to the streamwise adverse pressure gradient, the boundary layer upstream of the obstacle separates and forms horseshoe vortices that wrap around the obstacle. These horseshoe vortices being induced by the skewing of an incoming shear layer are classified as a secondary flow of the first kind and happen in both laminar and turbulent cases. In the case of a turbulent boundary layer, the system of vortices is unsteady. Time-averaged representation of the body wing junction generally shows a primary vortex which vorticity is the same as the incoming boundary layer as can be seen in Figure 2.1. Secondary vortices rotate in the opposite direction.

Ölçmen and Simpson [49] performed an experimental simulation of a 3:2 elliptical-nose NACA 0020 wing/body junction. Time-averaged oil visualization (Figure 2.2) shows the line of separation

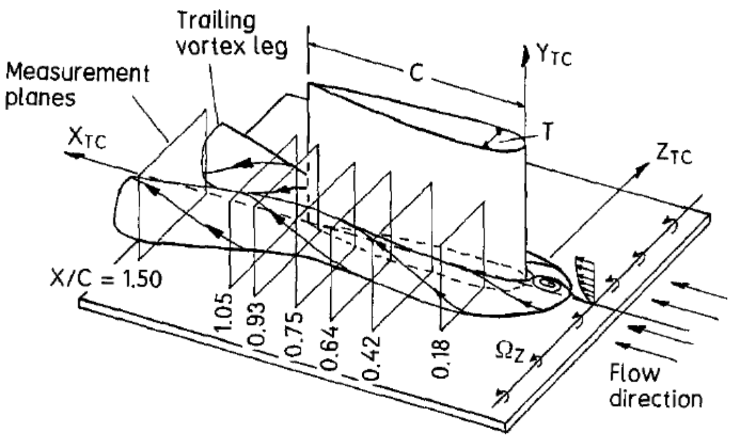

Figure 2.1: Sketch of the time averaged main horseshoe vortex from Fleming et al. [14]

around the wing. A saddle point is present at the intersection of the symmetry plane and this separation line. In addition, a line of low shear stress between the separation line and the wing can be observed. This line marks the limit between a region of low shear upstream of the line and a region of high shear closer to the wing.

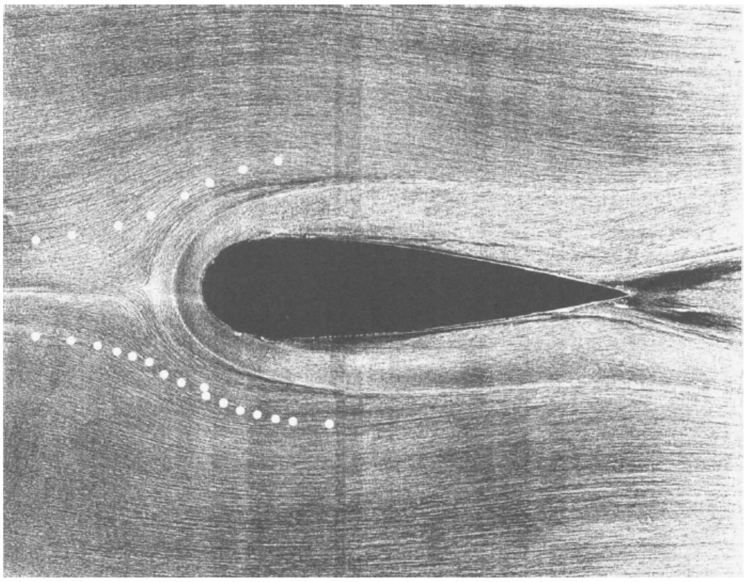

Figure 2.2: Oil visualization of the flow around a body-wing junction from Ölçmen and Simpson [49]

The horseshoe vortex system

In an extensive review study, Simpson [41] details the unsteady dynamics of the horseshoe vortices. The system of vortices go through different steps detailed by Kim et al. [21]: a primary vortex (PV) is formed upstream of the wing and stretched around it, then secondary vortexes (SV) are formed between the saddle point and the primary vortex, the PV moves closer to the wing and the SV merge with the PV. This causes an acceleration of the flow that stabilizes it. Finally, the flow becomes unstable and a new cycle restarts.

This behavior leads to one of the specificities of wing body junction ie the bimodal behavior detailed by Devenport and Simpson [9]. Near the center of the time-averaged main horseshoe vortex, the velocity switches aperiodically between a zero flow mode where the streamwise velocity is close to zero and a backflow mode where this velocity is negative as can be seen in Figure 2.3. Only the streamwise (U) and normal to the wall velocities (V) are concerned. The bimodal behavior is a low frequency phenomenon. According to Simpson [41], this behavior of the horseshoe vortex stops after the point of maximum thickness and the time average primary vortex shape appears more circular.

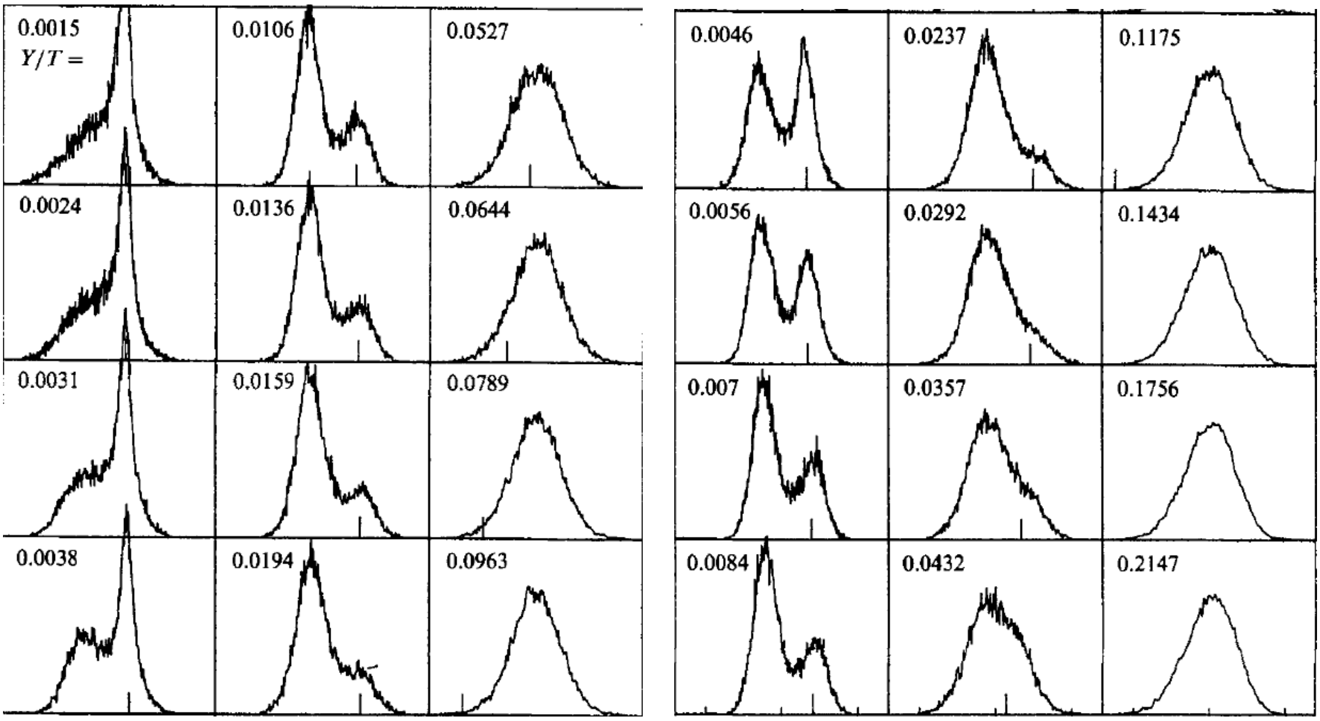

Figure 2.3: Probability-density functions of the streamwise velocity fluctuations at the primary vortex location from Devenport and Simpson [9]

Different factors influence the strength and mean location of the main horseshoe vortex. The shape of the object in the junction is of major importance. To account for this effect, Fleming et al. [13] introduced the bluntness factor BF:

$$BF = \frac{1}{2}\frac{R_0}{X_T}\left(\frac{T}{S_T} + \frac{S_T}{X_T}\right) \tag{2.1}$$

With T the maximum thickness of the wing, R_0 the leading edge radius, X_T the chordwise position of the maximum thickness and S_T the distance between the leading edge and the maximum thickness taken along the surface of the wing. High bluntness factor values lead to strong horseshoe vortex and bimodal behavior. The effect of the incoming boundary layer on the vortex system is taken into account by Fleming et al. [14] thanks to the momentum deficit factor:

$$MDF = (Re_T)^2(\theta/T) \tag{2.2}$$

With θ the boundary layer momentum thickness and Re_θ its associated Reynolds number. For high MDF, Fleming et al. [14] reported that the distance between the two legs of the vortex increases in the wake, and the center of the primary vortex moves closer to the wall. The angle of attack and swept of the wing have been observed to also play a role. Indeed, the bluntness of the wing increases with the angle of attack. Shizawa et al. [40] studied experimentally the influence of the angle of attack for a junction between a flat wing and a flat wing. On the suction side, they observed that the location of the vortex shifts further away from the wing to align with the freestream flow but that the distance from the wall remains the same, the peak turbulent kinetic energy is larger than on the pressure side but the size of the vortex is smaller. On the pressure side, the distance between the wing and the vortex center remains the same while the distance from the wall increases with the angle of attack. Ahmed and Khan [1] showed experimentally that a negative swept angle moves the separation line and time mean vortex closer to the body when a positive one moves it away from the body.

Corner separation

Under certain conditions of inflow and geometry, a corner separation can be observed on the trailing edge of the wing in junction flows. This behavior that has only been observed in turbulent cases is categorized as a secondary flow of the first kind. The separation happens mostly on the wing and does not seem to extend to the wall boundary layer as can be seen in the oil flow visualization Figure 2.4 of Kegerise et al. [20]. Barber [4] studied the link between boundary thickness and corner separation. He observed that a thin wall boundary layer creating a small horseshoe vortex leads to a large separation with an important dependence on the angle of attack. The situation is reversed in the case of a thick boundary layer. By comparing existing literature, Gand et al. [15] also point out that the bluntness of the object plays a role in the appearance of the corner separation. Sharp objects are associated with large corner separation and small HV. Although the BF and MDF factors effects have been verified in numerous experiments, there seem to be yet some other effects at play, as Gand et al. [15] pointed it out when observing no corner separation in contradiction to what was expected from the literature.

Figure 2.4: Oil-flow visualizations in the trailing-edge corner of the F6 wing from Kegerise et al. [20]

2.1.2. Numerical modeling of body wing junction

Numerous studies have modeled the body-junction flow. Apsley and Leschziner [3] provide one of the most extensive studies on the predictive capability of RANS models by comparing 12 RANS models to experimental data of a modified NACA0020. They compare linear eddy-viscosity, non-linear eddy-viscosity formulations, and differential stress models. They conclude on the superior accuracy of differential stress models compared to eddy viscosity models, both $k-g$ and $k-\omega$ SST models also providing good predictions for the mean quantities. However, the reverse flow predicted by these last two models is overestimated and the maximum of the turbulent kinetic energy is underestimated as can be seen in Figure 2.5d for the $k-\omega$ SST model. Out of all models, the $k-\epsilon$ based models, even the non-linear eddy viscosity ones give the worst results and present an abnormal representation of the turbulent kinetic energy k in front of the wing.

Jones and Clarke [18] also compare several RANS models and confirm the good performance of the $k-\omega$ SST model. They also recommend the Spalart-Allmaras model and the V2F model. Lee et al. [24] compare a set of RANS models very similar to the ones of Jones and Clarke [18] and conclude on a bad performance of $k-\epsilon$ models compared to all the other ones. Paciorri et al. [32], comparing

(a) Experimental results in Devenport and Simpson [9] taken from Ryu et al. [37]

(b) DES results in Paik et al. [33] taken from Ryu et al. [37]

(c) LES results from Ryu et al. [37]

(d) RANS results from Ryu et al. [37]

Figure 2.5: Comparison of RANS, DES and LES with experimental results for t.k.e upstream of a Rood wing from Ryu et al. [37]

a small number of RANS models, point out a relatively good performance of the Spalart-Allmaras model.

Gand et al. [15] in a comparative experimental and numerical study highlight the poor performance of all the RANS models studied (Spallart-Allmaras, Wilcox $k-\omega$, Menter $k-\omega$ SST and Speziale Reynolds Stress Model) as they all predict corner separation in complete contradiction to the experiment.

None of the RANS models studied by these different authors is able to capture the C-shape of the turbulent kinetic energy (t.k.e) in front of the wing.

Although a few RANS models seem to slightly outperform the others, all authors point out the limitations of these models for predicting the junction flows.

Paik et al. [33] performed a Detached Eddy Simulation (DES) of the wing body junction which leads to improved results compared to RANS and notably captures the bimodal behavior. However, mean kinetic energy and vorticity plots show that the location of the vortex in the symmetry plane is incorrectly predicted upstream of its location compared to the experiment (see Figure 2.5b). Two hypotheses could explain that the vortex is incorrectly predicted upstream of its true location: the RANS model used as a base for the DES (here Spallart Allmaras) or the input profile for the boundary layer.

Ryu et al. [37] perform an LES simulation of the wing–body junction flow experimentally studied by Devenport and Simpson [9] and demonstrate the superior performance of LES compared to RANS and DES. The C-shape of the turbulent kinetic energy of the mean primary vortex, its maximum strength and location are well captured as can be seen in Figure 2.5c. The corner vortex is also well represented. The good agreement between the results and experiments makes it possible for wall resolved LES to be used as ground truth data for data-driven techniques.

2.1.3. Adverse effects in junction flows

Junction flows can lead to several adverse effects. The unsteady behavior of the vortex system produces high variations of pressure and heat transfer. In the case of the bridge pier, the action of the vortex will scour the river bed leading to a possible collapse of the bridge (Simpson [41]). In addition, the interaction of the two nearly perpendicular boundary layers: the one developed on the wall and the one developed on the object, creates additional drag, namely interference drag. The total drag in the junction flow is indeed superior to the sum of the drag produced by the wall and body taken separately. Most systems previously studied focused on reducing or preventing the appearance of the horseshoe vortex.

Simpson [41] cites fillets as one of the more common designs used in the aerospace industry. Devenport et al. [8] reports that a fillet placed all around the wing does not seem to have a favorable effect on the junction flow: separation and bimodal behavior are still observed. No measurement is made on interference drag. However, Devenport et al. [10] concluded that a leading edge fillet prevents separation and the appearance of the horseshoe vortex at zero angle of attack. At high incidence, the favorable effect is reduced due to separation occurring on the pressure side. Without reliable RANS models for the design of body/wing junction the addition and shape of the fairing present on modern aircrafts also rely on the experimental knowledge of manufacturers.

Suction upstream of the wing, if rightfully placed, absorbs the incoming boundary layer, reducing the incoming vorticity and the strength of the vortex. Philips et al. [35] confirmed experimentally this effect at zero angle of attack and even found out that for a suction volumetric flow rate twice the flow rate of the wall boundary layer the vortex had completely disappeared. Barberis et al. [5] showed that the location of the suction influences a lot the efficiency of the device: suction of only $0.1U_\infty\delta^* T$ (with T the wing thickness, U_∞ the freestream velocity and δ^* the displacement thickness) was needed to remove the vortex if located between $x/T = -0.33$ to -0.10 , while if located at $x/T = -0.41$ a suction of $1.05U_\infty\delta^* T$ was needed. Both solutions are however likely to be dependent on the angle of attack.

Belligoli et al. [6] took a different focus in their study and aimed only at reducing the interference drag thanks to modifying the shape of the fuselage near the wing. The study introduced a different design for the junction named the Anti Fairing design obtained by aerodynamic shape optimization. In this design, the fuselage presents a dent around the protruding wing. Its maximum depth is approximately the one of the incoming boundary layer. This geometry was proved to reduce the drag better than the two fillets also tested by Belligoli et al. [6]. The action of the dent is different from the one of the fillet as it gives additional space to the vortex rather than seeking to reduce its size. As the vortex is still present in this case, the bimodal behavior is expected to also be present.

2.2. Machine Learning

Machine learning applied for fluid mechanics has gained interest in recent years thanks to the growing number of high fidelity data, both experimental and numerical as well as the improved performance of computers. Machine learning techniques are generally divided into three categories: supervised, unsupervised and semi-supervised learning. The distinction between the three categories relies on the amount of information given to the learning algorithm about the data. Training data are associated with a label for supervised learning when there is none in unsupervised learning. In semi-supervised learning, limited information can be given for example thanks to the interaction with the environment in reinforcement learning. In their review, Brunton et al. [7] cite dimensionality reduction methods such as Proper Orthogonal Decomposition (POD) as an unsupervised algorithm employed in fluid mechanics. Dynamic Mode Decomposition (DMD) introduced by Schmid [39] can also be categorized as unsupervised learning. Brunton et al. [7] point out that there is little work on unsupervised learning algorithm applied to fluid mechanics, most research being focused on supervised learning algorithms.

The main focus of this section will be restricted to supervised learning and the augmentation of RANS models thanks to machine learning. Most of the discussion can be transposed to the augmentation of LES models. This is because RANS is still widely used in industry due to its reasonable cost compared to techniques that resolve part of the scales such as LES or all of them like DNS. Additionally, numerous papers have been published regarding model augmentation via supervised learning as pointed out by the review paper of Duraisamy [11].

In the framework of supervised learning for RANS augmentation, the ensemble of features is called

η and the training data, which are spacial fields, $\beta(x)$. The goal of the machine learning algorithm is then to produce functional expressions $\beta(\eta)$ that are close representations of the training data $\beta(x)$. The data-driven models are then tested on a validation database to verify their predictive power. It has to be noticed that the function β is not necessarily deterministic nor explicit. Duraisamy et al. [12] and Duraisamy [11] pointed out several major aspects of the machine learning process: the form of the expression to be learned and the choice of features, the choice of the training data, the possibility to add physics-based constraints to the learning algorithm. To these different aspects, the learning algorithm itself can be added. In the following discussion, these aspects will be detailed and examples of their use in previous literature will be given.

2.2.1. Features selection

The choice of features η is of utmost importance, as well as the chosen architecture for β if one is selected. Duraisamy [11] advises that features should preferably be non-dimensional and respect invariance present in the equations. Local variables are suitable for generalizability but non-local variables have often proved to improve the solution. In the incompressible case, several studies (Schmelzer et al. [38], Ling et al. [27] ,Weatheritt and Sandberg [46]) have chosen to express the anisotropic part of the Reynolds tensor following Pope [36]'s tensors basis expression:

$$b^{\Delta} = \sum_{n=1}^{10} g^{n}(\lambda_1,...,\lambda_5)T^{n} \tag{2.3}$$

Where $\lambda_1...\lambda_5$ and T are functions of the mean strain rate S and rotation rate tensor R and can be found in Pope [36]. This integrity basis ensures that b^{Δ} is Galilean invariant and the Cayley-Hamilton theorem states that only ten tensors are needed to represent an eddy viscosity model that is a function of only S and R. Ling and Templeton [25] followed by Wang et al. [45] introduced physics-based features such as Q criterion or wall-distance based Reynolds number. Wu et al. [47] in order to have a more systematic approach compared to the previous work of Wang et al. [45] completed Pope's tensor basis formulation to include pressure influence and non-equilibrium effects by adding tensor and invariants based on ∇k and ∇P. Invariants were Galilean and rotational but not reflectional invariant. Three easily interpretable physical features were also added. This approach was later used in Kaandorp and Dwight [19] and Steiner et al. [44] adapting the additional physical features to the problem at stake.

The process of features creation described previously can lead to an important size of the library of features. Techniques can be performed to reduce the number of features in order to alleviate the computational load of the machine learning algorithm and to avoid redundant features. For instance, mutual information or cliqueing are some techniques used by Huijing et al. [17] and Steiner et al. [44]. Mutual information is a measure of how much a variable informs on another variable. Unlike a simple measure of correlation, this technique does not need a linear relationship but can detect any type of link. For two continuous random variables X and Y, their mutual information is expressed as :

$$MI(X,Y) = \int_x \int_y p(x,y) log \frac{p(x,y)}{p(x)p(y)} dxdy \tag{2.4}$$

MI can also be understood in terms of entropy which is a measure of the uncertainty of the random variable:

$$MI(X,Y) = H(X) - H(X|Y) \tag{2.5}$$

MI is then a measure of the reduction of uncertainty on X when Y is known. In practice, the probability distributions are not known. Steiner et al. [44] used a kernel density estimator to obtain their expressions. Cliqueing techniques are used to check if there are multiple colinearities between data. In Steiner et al. [44] only the simplest function is then retained.

2.2.2. Obtaining training data and features

The training data $\beta(x)$ and the training features can be obtained from different sources. Some of the choices made in literature are detailed here :

- DNS data or other high fidelity data. Using quantities directly obtained from high fidelity simulations has been a path taken by many authors. For instance, Ling et al. [26] and Weatheritt and Sandberg [46] used the Reynolds stress fields and features obtained from DNS simulations. This technique has the advantage to be easy to implement as the quantities are readily available if high fidelity data are provided. However, in addition to requiring full-field data, Duraisamy et al. [12] pointed out that the method is not model consistent as the features used for the training come from high fidelity database while the features used for prediction come from the RANS simulation.

- k-corrective frozen RANS by Schmelzer et al. [38]. Full-field data are also required. The anisotropic part of the tensor $a_{ij} = -2\nu_t S_{ij} = 2kb^0_{ij}$ is completed by a corrective term b^Δ_{ij} such that $a_{ij} = 2k(b^0_{ij} + b^\Delta_{ij})$. The transport equations that allow to solve for the turbulent viscosity ν_t are augmented with a corrective term for the production of turbulent kinetic energy (t.k.e) and the $k-\omega$ SST transport equations are modified into :

  $$\frac{Dk}{Dt} = P_k + R - \beta^* \omega k + \frac{\partial}{\partial x_j}\left[(\nu+\nu_t)\frac{\partial k}{\partial x_j}\right] \tag{2.6}$$

  $$\frac{D\omega}{Dt} = \frac{\gamma}{\nu_T}(P_k + R) - \beta\omega^2 k + \frac{\partial}{\partial x_j}\left[(\nu+\sigma_\omega\nu_t)\frac{\partial \omega}{\partial x_j}\right] + CD_{k\omega} \tag{2.7}$$

  With $P_k = min\left(-2k(b^0_{ij} + b^\Delta_{ij})\partial_j U_i, 10\beta^*\omega k\right)$ the production of t.k.e, and ω the specific dissipation rate. The other expressions and coefficients can be found in Menter [28]. To obtain the two corrective terms b^Δ_{ij} and R fields, the LES data is injected in the RANS equations. At each step, the turbulent kinetic energy deficit R is computed and fed back into the ω equation. The frozen corrective fields can be added in the RANS equation to be propagated.

- Field inversion (FI). To enforce model consistency, Parish and Duraisamy [34] introduced the Field Inversion approach. Having data points from high fidelity simulation Y^i, field inversion is performed to find models discrepancies $\beta_m(x)$ of the RANS equations and features that can produce the best approximation of Y^i. This problem can be expressed as an optimization of a cost function under the constraint of the realization of a PDE $R_a() = 0$:

  $$\min_{\beta^i} L[Y^i, Y^i_m(\beta^i_m)], \quad s.t \quad R_a(q_m, s_m, \beta_m(\eta_m, w)) = 0 \tag{2.8}$$

  With q_m and q_m coarse grained quantities in the PDE and w are parameters. Full-field data are not necessary as long as the data are sufficiently informative but the FI requires an adjoint-based optimization that can be challenging and costly. The first test of the technique for predictive purposes was made by Parish and Duraisamy [34] on turbulent channel flow cases. The model discrepancy β was introduced in the t.k.e equation of the $k-\omega$ model as a multiplicative term of the production of k. This technique was later extended to other turbulence models and cases such as a correction to the Spalart-Allmaras model for prediction of separation on 2D airfoils in Singh et al. [42].

2.2.3. Machine learning algorithm

Different options have been used for the learning algorithm that maps $\beta(x)$ into $\beta(\eta)$. A selection of the ones used in recent literature is recalled here:

- Neural networks (NN): Neural Networks consist of layers of neurons which behavior is inspired by biological neurons. Given several inputs, the neuron will generate an output thanks to nonlinear activation functions. Neural networks containing multiple layers are generally called deep Neural Networks. The layers in-between the input and output layers are often designated as hidden layers. One of the most common architectures, feed forward neural networks, as represented in Figure 2.6, has multiple layers where weighted outputs from a layer serve as inputs for the next one. Deep NNs allow to represent complex non-linear interactions, sometimes at the cost of interpretability. Weights in NNs can be found thanks to back-propagation techniques. Ling et al. [27] published a first proof of concept for using deep neural networks to obtain improved RANS models. Numerous other publications such as Singh et al. [42] employ deep NN.

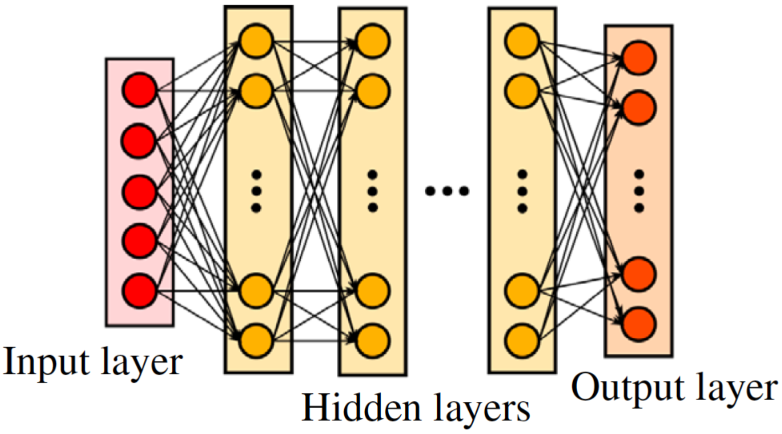

Figure 2.6: Architecture of feedforward network taken from Ling et al. [27]

- Random Forests (RF): Random forests are made of an ensemble of decisions trees. Each tree is trained with a randomly selected part of the training data and input features. The average or median prediction of the ensemble constitutes the prediction of the random forest. Random forests have the advantage of being relatively easy to implement, with only two parameters namely the tree depth and the size of the ensemble. Ling et al. [26] compared the performance of NN and RF and concluded that simpler algorithms like RF can give similar results than more complex ones (NN) if physics-based constraints are enforced.

- Genetic expression programming (GEP). Weatheritt and Sandberg [46] developed a method to obtain algebraic expression based on GEP. The algorithm starts with a random initial set of candidates functions. Candidate functions are divided into a function based on tensor called the chromosome and an optional scalar function called the plasmid. This allows to easily multiply several tensor expressions by the same scalar without having to find it several times. The plasmid and chromosome are coded as strings, each composed of a head of fixed length and tail. The algorithm consists of several rounds: at each round several subsets of candidates are selected. The fittest of each subset, as well as the global fittest, is retained. The retained candidates are then passed through operators that leave them unchanged or modify them with random mutations and combinations. The next round can then begin. The performance of the algorithm was tested for Periodic Hills and Backward Facing Step cases. Although the algorithm is non-deterministic, different runs of it have led to solutions with similar functions. Zhao et al. [48] extended the method by choosing the fittest function after an integrated RANS run. Cost functions can thus be chosen to be any desired variable. The stability of the model is enforced and this avoids the problem of inconsistencies pointed out by Duraisamy [11].

- Sparse regression. In the Sparse Regression of Turbulent Stress Anisotropy (SpaRTA) approach by Schmelzer et al. [38], an elastic net regression is performed on the library of candidates in order to choose the model functions while promoting the sparsity of the solution. The coefficients are then found with Ridge regression to favor small coefficients that generally tend to provide more stable RANS models. The advantage of such a method compared to neural networks, for example, is its interpretability and the possibility to obtain concise expressions for the correction to the Reynolds stress and production of turbulent kinetic energy.

Several authors also attempt to improve the quality of their machine learning algorithm by embedding physics constraints. This is the case of the various authors enforcing Galilean invariance of the features as seen earlier. Ling et al. [27] also performed a selection among the data-driven anisotropy based on the value of the components of the tensor and its eigenvalues.

A last note can be made on the universal nature of the data-driven models found by machine learning methods. Many authors such as Ling and Templeton [25],Weatheritt and Sandberg [46], Wang et al. [45] noted that found models can lack predictive accuracy when confronted to flow regions with different characteristics compared to the training data. The advice given for correcting this problem generally involves providing a more diverse training data set, extending the features library, and infusing physics constraints in the process. Wu et al. [47] point out that universality is only one possible goal as data-driven correction to classic turbulence models could be switched off for regions of the flow where the correction is not relevant. In this case, the challenge would be to determine a priori the area where the models can be used.

2.3. Research questions and objectives

2.3.1. Research Objective

The main research objective of this thesis deriving from the gaps identified in the literature study is:

> To produce a wall resolved LES of the Anti-Fairing body wing junction and to enhance the accuracy of RANS turbulence models in the case of body wing junction flows using a data-driven turbulence modeling approach (namely SpaRTA)

The novelty of this research lays in the generation of a wall resolved LES of the Anti-Fairing case and the application of the SpaRTA methodology on body/wing junction flows, a case that has not been tested before.

First, a LES simulation of the Anti-Fairing wing body junction must be performed, analyzed, and verified. The next sub-goal is to understand the SpaRTA methodology thanks to literature study and tests on 2D test flows. The optimum baseline RANS simulation must then be selected. The last sub-goal to achieve before the machine learning part is the obtention of the training data with the k-corrective frozen approach. The next objective is to apply and modify if needed the SpaRTA methodology to obtain data augmented RANS models. Provided that relevant data-driven models are found they can be inserted in OpenFoam and their prediction compared to LES data.

2.3.2. Research Question(s)

From the main research objective, two main questions and their associated subquestions can be derived.

- What is the impact of the Anti-Fairing on the junction flow?

  - Is the LES presenting the expected characteristics of a body wing junction?
  - Is the LES of the Anti-Fairing design in agreement with experiments from Belligoli et al. [6]?
  - How does it compare to the wall resolved LES of the flat plate and Rood wing of Alberts [2]?
  - Does this new simulation provide additional insights into the working principle of the Anti-Fairing design?

- Can the data-driven technique SpaRTA be applied to obtain enhanced RANS turbulence models for the body wing junction?

  - What is the best RANS model to augment with corrective terms? What are the limitations of these models to overcome with the data-driven models?
  - Is the k-corrective frozen approach able to provide informative corrective terms for RANS models?
  - How to select the training data for SpaRTA? Should part of the high fidelity data be removed for the machine learning part?
  - What are the invariants and integrity basis tensors and physical features needed for the library of the SpaRTA algorithm?
  - Will the SparRTA methodology be able to find the relevant features to model wing/body junction flows? Does the SpaRTA algorithm need to be modified for this specific case?
  - How do the results of the data-driven RANS models compare to LES results?
  - What does the algebraic expression for the correction to the Reynolds stress and turbulence kinetic energy tell us about the physics of body wing junction?

3

Methodology

In this chapter, the different techniques and algorithms used are discussed. The first stage of the work consists in generating a wall resolved LES of the AntiFairing body wing junctions. Alberts [2] previously performed a wall resolved LES of the junction between a flat plate and the Rood wing. The present LES will be used to compare the Anti-Fairing junction with the baseline case of Alberts [2] and as part of a database of training data for machine learning approaches. The methodology used in the LES simulation is detailed. The second stage of the work is to generate turbulent data-driven models for body-wing junction flows. To this effect, the k-corrective frozen approach is used to generate corrective fields to the RANS equations, then the SpARTA methodology is used to generate the models.

3.1. Large Eddy Simulation

In this section, the details of the LES are given. First, the governing equations of LES are recalled. Then the geometrical set-up and boundary conditions are described. Finally, the mesh information and the settings of the simulation are provided.

3.1.1. Governing Equations

In fluid dynamics, the Navier-Stokes equations are used to describe the motion of a flow. The equations for incompressible Newtonian fluids are:

$$\begin{gathered}\frac{\partial U_i}{\partial x_i} = 0 \\ \frac{\partial U_i}{\partial t} + \frac{\partial U_i U_j}{\partial x_j} = -\frac{1}{\rho}\frac{\partial P}{\partial x_i} + \frac{\partial}{\partial x_j}\left[\nu\left(\frac{\partial U_i}{\partial x_j}\right)\right]\end{gathered} \tag{3.1}$$

With U_i is the i-th component of the velocity, P the pressure, and ν the viscosity. Direct Numerical Simulation (DNS) of the Navier-Stokes equations is not possible in most cases due to the high computational cost of their resolution. Indeed, it would require the cells to have a size that is close to the smallest scale of turbulence ie Kolmogorov microscales where turbulent kinetic energy is dissipated. Large Eddy Simulation (LES) constitutes the second most accurate technique as it resolves the largest scales of turbulence and models only the influence of the non-resolved smallest scales on the larger scales. The LES equations in Equation 3.2 are obtained by applying a filter to the Navier-Stokes ones, each component of the velocity U_i is decomposed between the filtered $\overline{U_i}$ and the sub-grid u''_i as $U_i = \overline{U_i} + u''_i$. The same filtering is applied to the pressure.

$$\begin{gathered}\frac{\partial \overline{U}_i}{\partial x_i} = 0 \\ \frac{\partial \overline{U}_i}{\partial t} + \frac{\partial \overline{U}_i \overline{U}_j}{\partial x_j} + \frac{1}{\rho}\frac{\partial \overline{P}}{\partial x_i} - \nu\frac{\partial^2 \overline{U}_i}{\partial x_j \partial x_j} = -\frac{\partial \tau_{ij}}{\partial x_j} \\ \tau_{ij} = \overline{U_i U_j} - \overline{U}_i \overline{U}_j\end{gathered} \tag{3.2}$$

τ_{ij} is the sub-grid scale (SGS) tensor and needs to be modeled in order to close the system.
Filtering can be done in an explicit or implicit manner. In the implicit case , the observation is made that the numerical scheme can be used to dissipate the energy in a similar way the smallest scales would do. In the explicit case, the expression for the SGS model of τ_{ij} is computed. Here, an explicit LES is chosen. One of the most common approach to model explicitly the SGS tensor is the eddy viscosity approach where :

$$\tau_{ij} = \frac{1}{3}\tau_{kk} - 2\nu_t\overline{S_{ij}} \tag{3.3}$$

Where $\overline{S_{ij}}$ is the resolved rate-of-strain tensor and ν_t the turbulent viscosity.
Smagorinsky [43] introduced the first SGS model where $\nu_t = (C_S\Delta)^2|\overline{S_{ij}}|$, with C_S the Smagorinsky constant and Δ the filter width. This simple model needs some ad-hoc fix close to the walls such as van Driest Damping functions.
In the current approach, following Alberts [2] the Wall-Adapting Local Eddy-viscosity (WALE) SGS model proposed by Nicoud and Ducros [31] is chosen. The WALE modeled is an improved SGS model compared to the Smagorinsky [43] one that succeeds in obtaining the correct asymptotic behavior $\nu_t = O(y^3)$ close to the wall. This property is highly desirable in the case of body-wing junctions where the distinctive features of the flow appear in the boundary layer. The sub-grid scale viscosity is then:

$$\nu_t = (C_S\Delta)^2 \frac{(S^d_{ij}S^d_{ij})^{3/2}}{(\bar{S}_{ij}\bar{S}_{ij})^{5/2} + (S^d_{ij}S^d_{ij})^{5/4}} \tag{3.4}$$

With $S^d_{ij} = \frac{1}{2}(\overline{g_{ij}}^2 + \overline{g_{ji}}^2) - \frac{1}{3}\delta_{ij}\overline{g_{kk}}^2$ being the traceless symmetric part of the square of the velocity gradient tensor $\overline{g_{ji}}$.

3.1.2. Geometry and computational domain

Geometry

The geometry studied for the LES is the one of the AntiFairing introduced by Belligoli et al. [6]. More precisely, it is composed of a Rood wing with 3:2 elliptical wing nose and a NACA0020-tail, attached on a flat plate with a dent around the wing. The wing thickness is $T = 0.0717\ m$ and the chord length is $c = 4.254T$. The streamwise direction is referred to as X, the vertical direction as Y and the longitudinal direction as Z. The maximum depth of the concave dent is of $0.21T$. It extends from $X/T = -3.5$ to $X/T = 7$ with a half-width of $2.9T$. The resulting body wing junction can be seen in Figure 3.1a. The baseline geometry is composed of a Rood wing mounted on a flat plate and can be seen in Figure 3.1b.

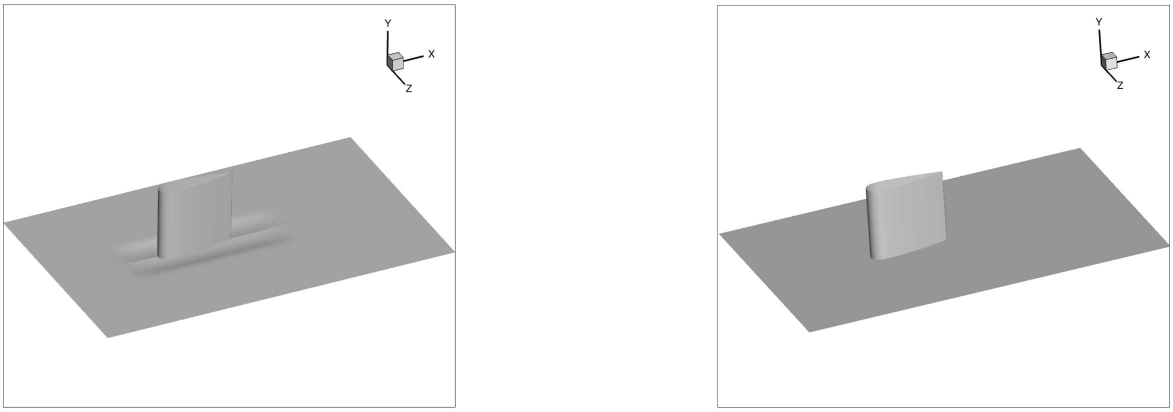

(a) Anti-fairing body wing junction

(b) Baseline body wing junction

Figure 3.1: Baseline an Anti-Fairing body wing junction geometries

Computational domain

The computational domain is composed of a rectangular box around the wing. The inlet is located $1.4c$ away from the leading edge. The outlet is $2.35c$ away from the trailing edge. The sides are located at $1.5c$ of the symmetry plane where $Z = 0$. The bottom includes the Anti-Fairing region. The top is located at $4T$ which should avoid any artificial effect of this boundary to influence the region close to the junction. These dimensions are similar to the work of Alberts [2].

Boundary conditions

The choice of the boundary conditions is made following Alberts [2] and is illustrated in Figure 3.2. The sides and top part surfaces have a symmetry condition. The wing and bottom including the anti-fairing dent have a no-slip condition. The outlet has a zero pressure condition. The INLET TOP, located above the input boundary layer has a uniform free stream velocity of $U = 27\ m/s$. Finally, the INLET BOT is a time-wise and spatially varying boundary condition obtained thanks to a precursor. The thickness of this boundary layer is $\delta_{inlet} = 0.0316m$. The precursor data were generated by Alberts [2] by sampling the inlet of a turbulent channel flow (TCF). The dimensions of the TCF are a height of $h_p = 2\delta_{inlet}$, a width of $b_p = 3c$ equals to the one of the main simulation, and a length of $l_p = 8\delta_{inlet}$. The inlet and outlet of this turbulent channel flow are coupled. The velocity flow is controlled in OpenFoam by the *meanVelocityForce* controller which imposes a bulk velocity U_b calculated according to :

$$U_b = \frac{1}{h_p} \int_0^{h_p} < u(y) > dy \tag{3.5}$$

Where $< u(y) >$ is the time-averaged streamwise component of the velocity. An interpolation with the nearest neighbor technique step is performed between the inlet of the TCF and the precursor of the main simulation because the mesh of the inlet of the TCF is different from the one of the inlet of the Anti-Fairing simulation . This is done thanks to the tool *eddylicious* suggested by Mukha and Liefvendahl [30] and also used by Alberts [2].

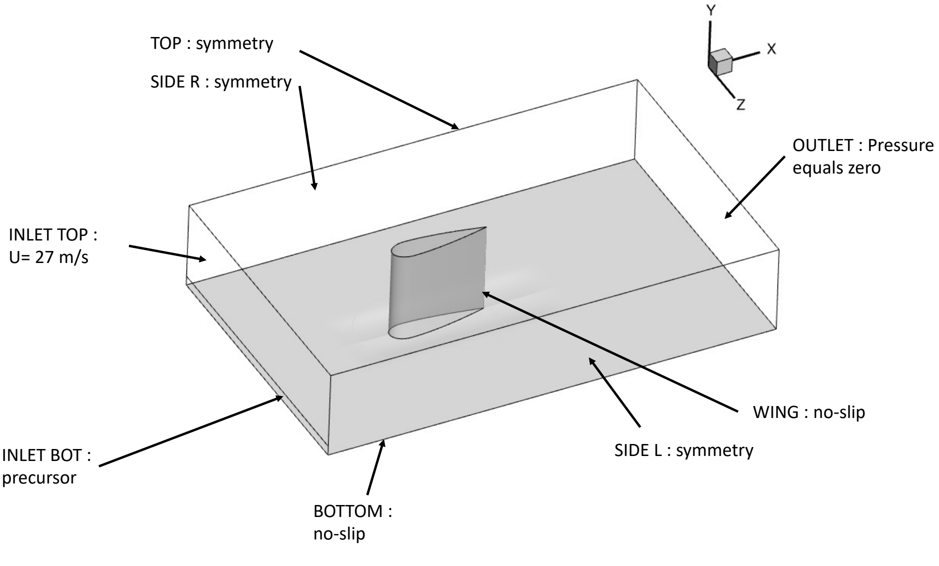

Figure 3.2: Computational domain and boundary conditions

3.1.3. Mesh

The structured mesh is generated with ANCYS ICEM. One of the main interests of this LES is to perform a wall resolved simulation of the anti-fairing wing body junction as the work of Kumar [23] proved the limitation of using wall modeled LES for junction flows. The domain is separated into 120 blocks in order to control the cell size more accurately.

The total number of cells is 61.7 million. To resolve the flow up to the walls, the first cell is located at $y \approx 1e-5$ so that $y+ < 1$ on the wing and bottom wall. The cell size progressively increases as the distance from the wing and bottom wall also increases. The resulting mesh is shown in Figure 3.3 and Figure 3.4. It is very similar to the one of Alberts [2].

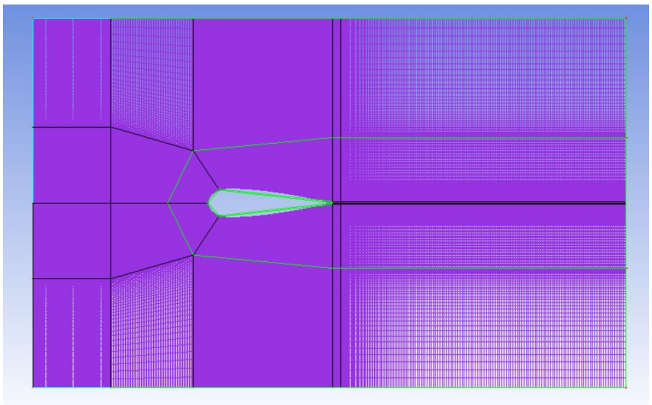

Figure 3.3: Top view of the mesh for the Antifairing case

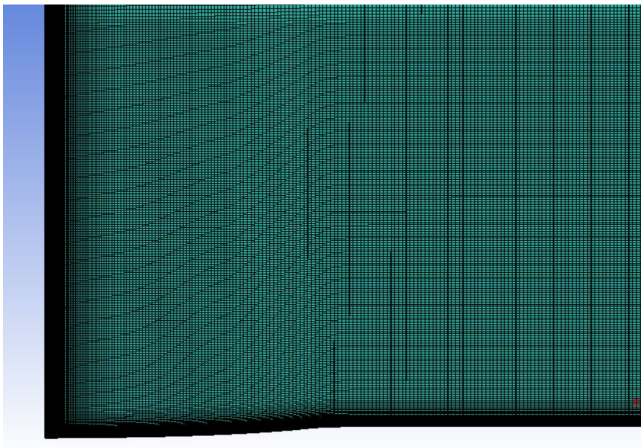

Figure 3.4: Cross section of the mesh in the symmetry plane before the wing

3.1.4. Solver details

The solver used for this study is the PIMPLE solver of OpenFoam 4. It is a solver for transient incompressible flow. The pressure equation is solved with the Preconditioned Conjugate Gradient (PCG) solver with a Diagonal Incomplete-Cholesky (DIC) preconditioner. The other equations are solved using the smoothSolver of OpenFoam with the GaussSeidel smoother. The velocity and pressure equations are solved two times within one timestep and the final tolerance is set to $1e-6$ and $1e-8$ for the velocity.

For the numerical schemes of each term, the following settings are taken. The discretization scheme for the time derivative is second order implicit. The gradients are computed using the Gauss linear method. The convective terms use the Gauss LUST $grad(U)$ for U. The laplacian uses the Gauss linear corrected method.

The time-step for the simulation is taken to be $\Delta t = 1.85e-6\ s$ to ensure that the CFL condition remains below 1 during the full simulation. The CFL is defined as :

$$CFL = \frac{U\Delta t}{\Delta x} \tag{3.6}$$

With U the cell-wise velocity at a given time step, and Δx the cell size. The convergence of the solution is monitored thanks to probes located at several points in the domain. The result for two probes in the symmetry plane is shown in Figure 3.5 and Figure 3.6. The first probe is located at $X/T = -1.3947$ and $Y/T = 0.0697$ and the second probe is located closer to the wing but further to the wall at $X/T = -0.1395$ and $Y/T = 0.3487$. Because the second probe is located closer to the wing, it is possible to observe that the mean pressure is larger than the one of the first probe. A transient is present in the first $0.2s$ of the simulation. It can also be observed that low levels of turbulence are observed during $0.02s$ around 1.015. This is likely to be caused by an incorrect reading of the precursor by OpenFoam when adding time folders in the precursor folder. The simulation recovers then almost immediately. Results shown in Chapter 4 should not be impacted by this error in the simulation as they are taken from $t = 1.08s$.

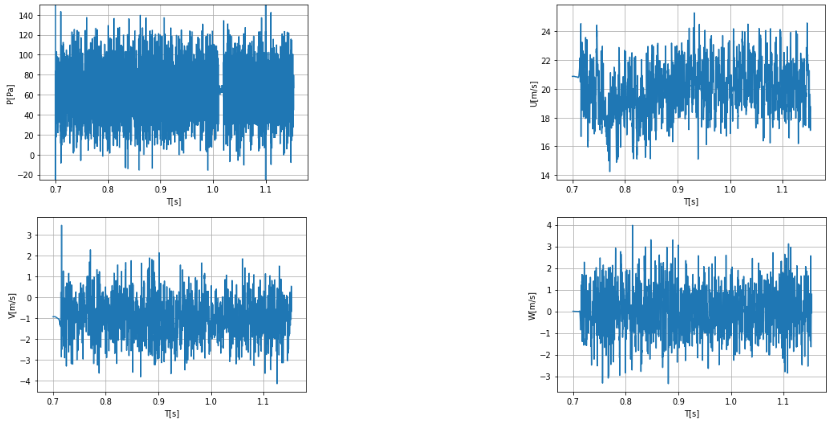

Figure 3.5: Instantaneous fields $X/T = -1.3947$ and $Y/T = 0.0697$

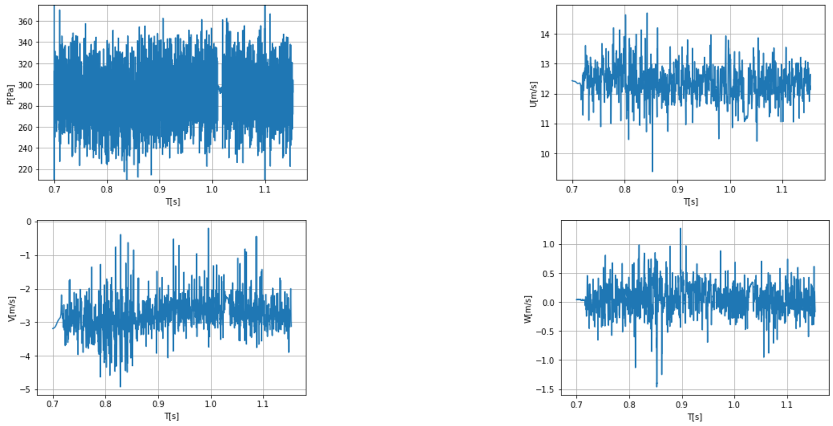

Figure 3.6: Instantaneous fields $X/T = -0.1395$ and $Y/T = 0.3487$

3.2. Data driven models

In this section, the methodology to obtain data-driven models is described. The first step consists in obtaining training data in the form of corrective terms for the RANS equations. This method is called the k-corrective frozen approach. The training data are then selected. The library of functions that will be used to model the corrective terms is generated. Additional steps to limit the size of the library and select relevant components are performed. The fifth step consists in generating the appropriate models following the SpaRTA method. If informative models are found, a final step (not performed here) consists in testing the performance of the obtained models by implementing them in OpenFoam.

3.2.1. k-corrective frozen RANS

The present work and the one of Alberts [2] provide two wall resolved simulations of the body wing junction with different geometries. This set of data can be used as ground truth for data driven approach.

The RANS equations do not predict accurately the features of the body-wing junction. The discrepancy between LES and RANS can be overcome by adding two corrective terms to the $k-\omega$ SST RANS model: one added to the turbulent kinetic energy equation , and an other one added to the Reynolds stress. The first step consists of generating the training fields namely R and b^{Δ}_{ij} thanks to the k-corrective frozen method developed by Schmelzer et al. [38].

The continuity and momentum equations for RANS in the incompressible case are :

$$\nabla.U = 0 \tag{3.7}$$

$$U_j \partial_j U_i = \partial_j \left[-1/\rho P + \nu \partial_j U_i - \tau_{ij} \right] \tag{3.8}$$

ρ, U, P and ν are the density, average velocity, generalized pressure and molecular viscosity.

The Reynolds stress $\tau_{ij} = \overline{u'_i u'_j}$ is a function of the fluctuations of the velocity. The task of all RANS models is to propose a model for this tensor to close the equations. In the case of eddy viscosity models such as Menter $k-\omega$ SST , the Reynolds stress is expressed as $\tau_{ij} = 2k(-\frac{\nu_t}{k} S_{ij} + \frac{1}{3}\delta_{ij})$ with S_{ij} the mean strain rate tensor, and k the turbulent kinetic energy. The $k-\omega$ SST model is a two equation model: a turbulent kinetic energy (t.k.e) equation and a specific dissipation rate equation close the model and allow to compute ν_t.

In the k-corrective frozen RANS approach, the anisotropic part of the Reynolds stress tensor $a^0_{ij} = -2\nu_t S_{ij} = 2kb^0_{ij}$ is completed by a corrective term b^{Δ}_{ij} such that:

$$a_{ij} = 2k(b^0_{ij} + b^{\Delta}_{ij}) \tag{3.9}$$

In addition, the transport equations are augmented with a corrective term R . Equation 3.10 and Equation 3.11 show the original $k-\omega$ SST transport equations (in black) with their modifications (in red).

$$\frac{Dk}{Dt} = P_k + R - \beta^* \omega k + \frac{\partial}{\partial x_j}\left[(\nu + \nu_t) \frac{\partial k}{\partial x_j} \right] \tag{3.10}$$

$$\frac{D\omega}{Dt} = \frac{\gamma}{\nu_T}(P_k + R) - \beta \omega^2 k + \frac{\partial}{\partial x_j}\left[(\nu + \sigma_\omega \nu_t) \frac{\partial \omega}{\partial x_j} \right] + CD_{k\omega} \tag{3.11}$$

$$P_k = min\left(-2k(b^0_{ij} + b^{\Delta}_{ij}) \partial_j U_i, 10\beta^* \omega k \right) \tag{3.12}$$

$P_k = P^0_k + P^{\Delta}_k$ is the production of t.k.e, and ω the specific dissipation rate. The other expressions and coefficients can be found in Menter [28].

To obtain the b^{Δ}_{ij} and R fields, the LES fields U, k and τ_{ij} are injected in the RANS equations. At each step, the turbulent kinetic energy deficit R is computed and fed back into the ω equation. This method was first implemented by Schmelzer et al. [38] for OpenFoam 2.4.0 and actualized for OpenFoam 4 in this work.

One important detail must be noted as this step: in the initial work of Schmelzer et al. [38], no constraint was added to the RANS equations and the approach was taken on the same domain and mesh as the LES. However, in this work, a minimum on ω was imposed to avoid unphysical high oscillations of ω that impact the calculation of the deficit in t.k.e. This minimum was chosen to be the value of the frozen ω in the freestream region at the inlet. Additionally, unphysical values close to the inlet artificially raise the value of the frozen ω when the method is applied to the full LES domain. To avoid this effect the frozen approach was performed on a smaller domain where the region with $X < 0.4m$ is removed. With these modifications, it was made possible to use the k-corrective frozen approach successfully. Because of these modifications, any values for R and b^{Δ}_{ij} that are close to the regions where the limiter on ω is activated cannot be used in the following steps. It was observed that these regions are not occurring in the boundary layer. As the current study is mostly interested in capturing the behavior of the characteristics of junctions flows that appear close to the wall such as separation and horseshoe vortices, this limitation is not perceived as an obstacle to obtaining informative data-driven models. The training data will only be used for the boundary layer region.

3.2.2. Selection of training dataset

The training of the data-driven models is done with the data of the baseline case. The Anti-Fairing configuration can be used in further research on data-driven modeling of junction flows. The training fields b^{Δ}_{ij} and R obtained thanks to the present k-corrective frozen RANS on the smaller mesh contains about 60 million cell values. As mentioned earlier the region outside the boundary layer is of little interest and contains small zones of unphysical values, discarding these regions allows to reduce the size of the two training fields. However, this reduction is not sufficient to have reasonably small fields. The boundary layer was thus divided into several regions of interest where the characteristics of the flow are different.

The first one is a rectangular region located at $-0.35 < X < -0.05$ and $-T < Z < T$ before any separation or vortex creation. It has been noted that the boundary layer arriving on the wing is already different between the RANS and LES simulations. Additionally, a second region around the vortex and before the maximum thickness of the wing can be selected. Figure 3.7a and Figure 3.7b shows the selected points (in red) and the vortex (in blue) for this second region.

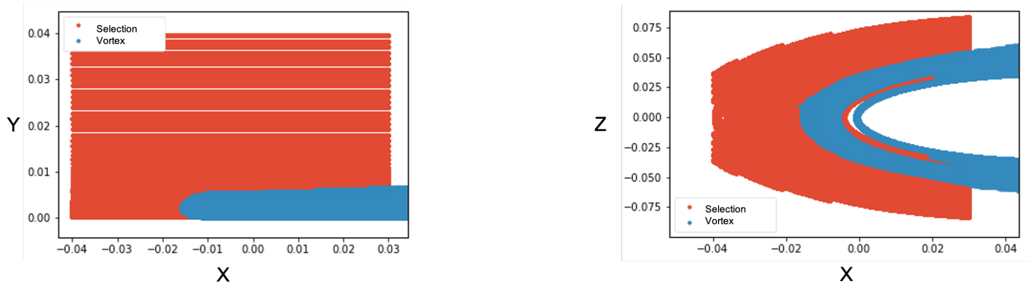

(a) XY view of the second region of training

(b) XY view of the second region of training

Figure 3.7: Second region of training

The regions past the maximum thickness are of lesser interest as they do not see the creation of the typical features of the body wing junctions. Corrections learned upstream of the maximum thickness should be sufficient to capture the appropriate characteristics .

3.2.3. Library of candidate functions

Once the training data has been generated and selected, the next step of data driven approach consists in defining the way the models that approximate these data will be constructed.

In the effective viscosity hypothesis, the Reynolds stress is a function of the rate of strain and scalar quantities only. Pope [36] determined that the Reynolds stress can be expressed as a polynomial of

Notation	Description	Raw feature	Normalization
q_Q	Q criterion	$0.5(\lVert\Omega\rVert^2 - \lVert S\rVert^2)$	$\lVert S\rVert^2$
q_{TI}	Turbulence intensity	k	$0.5U_i^2$
q_d	Wall distance based Reynolds number	$\frac{\sqrt{k}d}{50\nu}$	–
$q_{dp/ds}$	Pressure gradient along streamlines	$U_k\frac{\partial P}{\partial x_k}$	$\sqrt{\frac{\partial P}{\partial x_j}\frac{\partial P}{\partial x_j}U_iU_i}$
q_T	Ratio of mean turbulent to mean straintime scale	$\frac{1}{\omega}$	$\lVert S\rVert$
q_ν	Viscosity ratio	ν_t	100ν
q_V	Vortex stretching	$\sqrt{\omega_j\frac{\partial U_i}{\partial x_j}\omega_k\frac{\partial U_i}{\partial x_k}}$	$\lVert S\rVert^2$
q_P	Ratio of pressure normal stresses to shear stresses	$\frac{\sqrt{\frac{\partial P}{\partial x_i}\frac{\partial P}{\partial x_i}}}{\left\lvert\rho U_i\frac{\partial U_i}{\partial x_i}\right\rvert}$	–
$q_\perp$	Nonorthogonality between velocity and its gradient	$\lvert U_iU_j\rvert\frac{\partial U_i}{\partial x_j}$	$\sqrt{U_n^2U_i\frac{\partial U_i}{\partial x_j}U_m\frac{\partial U_m}{\partial x_j}}$
q_γ	Shear parameter	$\left\lVert\frac{\partial U_i}{\partial x_j}\right\rVert$	ω

Table 3.1: Additional physical features

ten tensors which coefficients depend on five invariants. Following this approach, Schmelzer et al. [38] expressed the corrective term to the Reynolds stress b_{ij}^{Δ} as :

$$b_{ij}^{\Delta} = \sum_{n=1}^{N=10} T_{ij}^{(n)}\alpha(\lambda_1,...,\lambda_5) \tag{3.13}$$

$T_{ij}^{(n)}$ are Pope [36] 's tensor basis based on the normalized mean strain rate $\widetilde{S_{ij}} = S_{ij}/\omega$ and normalized rotation rate tensor $\widetilde{\Omega_{ij}} = \Omega_{ij}/\omega$ and are defined as :

$$\begin{aligned}
&T_{ij}^{(1)} = \widetilde{S_{ij}} && T_{ij}^{(2)} = \widetilde{S_{ij}}\widetilde{\Omega_{ij}} - \widetilde{\Omega_{ij}}\widetilde{S_{ij}}\\
&T_{ij}^{(3)} = \widetilde{S_{ij}}^2 - \frac{1}{3}\delta_{ij}\{\widetilde{S_{ij}}^2\} && T_{ij}^{(4)} = \widetilde{\Omega_{ij}}^2 - \frac{1}{3}\delta_{ij}\{\widetilde{\Omega_{ij}}^2\}\\
&T_{ij}^{(5)} = \widetilde{\Omega_{ij}}\widetilde{S_{ij}}^2 - \widetilde{S_{ij}}^2\widetilde{\Omega_{ij}} && T_{ij}^{(6)} = \widetilde{\Omega_{ij}}^2\widetilde{S_{ij}} + \widetilde{S_{ij}}\widetilde{\Omega_{ij}}^2 - \frac{2}{3}\delta_{ij}\{\widetilde{S_{ij}}\widetilde{\Omega_{ij}}^2\}\\
&T_{ij}^{(7)} = \widetilde{\Omega_{ij}}\widetilde{S_{ij}}\widetilde{\Omega_{ij}}^2 - \widetilde{\Omega_{ij}}^2\widetilde{S_{ij}}\widetilde{\Omega_{ij}} && T_{ij}^{(8)} = \widetilde{S_{ij}}\widetilde{\Omega_{ij}}\widetilde{S_{ij}}^2 - \widetilde{S_{ij}}^2\widetilde{\Omega_{ij}}\widetilde{S_{ij}}\\
&T_{ij}^{(9)} = \widetilde{\Omega_{ij}}^2\widetilde{S_{ij}}^2 + \widetilde{S_{ij}}^2\widetilde{\Omega_{ij}}^2 - \frac{2}{3}\delta_{ij}\{\widetilde{S_{ij}}^2\widetilde{\Omega_{ij}}^2\} && T_{ij}^{(10)} = \widetilde{\Omega_{ij}}\widetilde{S_{ij}}^2\widetilde{\Omega_{ij}}^2 - \widetilde{\Omega_{ij}}^2\widetilde{S_{ij}}^2\widetilde{\Omega_{ij}}
\end{aligned} \tag{3.14}$$

The brace indicates the trace of the vector. $\alpha(\lambda_1,...,\lambda_5)$ is a scalar function of the five invariants depending also on S and Ω.They are defined as:

$$\lambda_1 = \{\widetilde{S_{ij}}^2\} \quad \lambda_2 = \{\widetilde{\Omega_{ij}}^2\} \quad \lambda_3 = \{\widetilde{S_{ij}}^3\} \quad \lambda_4 = \{\widetilde{\Omega_{ij}}^2\widetilde{S_{ij}}\} \quad \lambda_5 = \{\widetilde{\Omega_{ij}}^2\widetilde{S_{ij}}^2\} \tag{3.15}$$

Previous studies show that using only these five invariants does not provide sufficiently good models in practice. Ling and Templeton [25], Wang et al. [45] and Steiner et al. [44] listed additional physical features that are of interest for turbulence modeling. They are listed in Table 3.1.

Most of the features in Table 3.1 are frequently used in fluid mechanics. For instance, the Q criterion q_Q is a metric that compares the vorticity magnitude to the magnitude of the rate of strain. It is especially useful in characterizing the vortex structures of the flow. The wall distance based Reynolds number indicates the difference between boundary layers and shear flows. The selection of the relevant features for the present case is described in subsection 3.2.4.

The turbulent kinetic energy deficit R can be seen as a term of production of energy in the k equation and be written is the same form as P_k, so

$$R = 2kb^R_{ij}\partial_j U_i \tag{3.16}$$

With $b^R_{ij} = \sum_{n=1}^{N} T^{(n)}_{ij}\alpha^R(q_1,...,q_F)$ and q_n an ensemble of features.

Expressing the deficit of turbulent kinetic energy as a production of energy was not sufficient to create informative models in the present case. Thus, it was decided to use a more general form as in the work of Steiner et al. [44] . The turbulent kinetic energy deficit R is then written:

$$R = 2k\sum_{n=1}^{N} T^{(n)}_{ij}\alpha^R(q_1,...,q_F)\partial_j U_i + \omega k\beta^R(q_1,...,q_F) \tag{3.17}$$

Expressed in this way, R cannot be seen anymore as a correction to the production of t.k.e. As a consequence, Equation 3.11 should be modified so that $\frac{\gamma}{\nu_t}$ does not multiply R. In this work, to avoid recomputing two times the k-corrective-frozen approach, this argument was ignored in the following.
As difficulties were encountered to find models for b^Δ_{ij}, only its impact on the transport equations is modeled and only models for $P^\Delta_k = -2k(b^\Delta_{ij})\partial_j U_i$ are investigated .
A library of candidates functions B for α, α^R and β^R is generated by combining the invariants and physical features together according to the following process:

- Exponentiation step: In the temporary library B1, each invariant and physical feature is raised to the power of n, with n in [0.5,1,2]
- First combination : In B2, each item of B1 is multiplied by the items of B1 following it in the list.
- Second combination : In B3, each item of B2 is multiplied by each item of B1.
- Concatenation: Finally B is made of B1, B2 and B3 and is cleaned so that redundant functions are removed.

A library C for the terms of R and P^Δ_k is built by multiplying each term of B by $2kT^{(n)}_{ij}\partial_j U_i$ or ωk.

3.2.4. Feature reduction

The previous approach leads to an important number of candidate functions. Three steps are performed to reduce the library . First, mutual Information introduced by Steiner et al. [44] was used to determine the importance of the different features. Mutual information is a measure of the amount of information one variable X gives about another variable Y and is formally expressed as :

$$MI(X,Y) = \int_x\int_y p(x,y)log\frac{p(x,y)}{p(x)p(y)}dxdy \tag{3.18}$$

$$= H(X) + H(Y) - H(X,Y) \tag{3.19}$$

With H the entropy of the variable. For variables that are completely independent, MI is zero. Features that have a high mutual information with the training data will be selected for the rest of the study. In this work, following Goderie [16], the probability densities are evaluated thanks to the k-nearest neighbor method by Kraskov et al. [22]. For the variables X and Y , the mutual information can be obtained from the N samples of each variable. For a given k, Kraskov et al. [22] take the distance from a given point $z_i = (x_i, y_i)$ to its k neighbor $z'_i = (x'_i, y'_i)$ as :

$$\epsilon(i)/2 = max(||x_i - x'_i||, ||y_i - y'_i||). \tag{3.20}$$

$n_x(i)$ is the number of points satisfying $||x - x_i|| < \epsilon(i)/2$ and $n_y(i)$ is number of points satisfying the same condition on y. Kraskov et al. [22] show that using the approximation that $p(x)$ is constant over the ball of radius $\epsilon(i)/2$ and centerx_i, the mutual information can be expressed as :

$$MI(X,Y) = \psi(k) - \frac{1}{N}\sum_{i}^{N} \psi(n_x(i)+1) + \psi(n_y(i)+1) + \psi(N) \tag{3.21}$$

With ψ the digamma function. k is set to 3, as in Goderie [16] because Kraskov et al. [22] advise to choose k between 2 and 4. The MI is finally normalized by the target self MI. Self MI being different from ∞ due to the limited number of samples N and the assumption on $p(x)$ over the $\epsilon(i)$ ball.

Secondly, a limitation is imposed on the order of the library functions. The maximum order of each polynomial in B is chosen by the author to be lesser than 3.
Finally, once the library is built using only the features, invariants and tensors which have the most important MI with the target data, the number of functions in the library is significantly reduced by using cliqueing. Cliqueing was introduced by Steiner et al. [44] and Huijing et al. [17] to eliminate functions with important correlation to other functions of the library. In the present case, the cliqueing technique was able to reduce the library by a factor of 4 to 6. In graph theory, a clique is a complete subgraph of correlated functions. The threshold for correlation is set to 0.99 here. Only the function with the lowest complexity is selected in each clique.

3.2.5. Sparse Regression of Turbulent Stress Anisotropy

The process of creating the models is separated into a model discovery phase where the relevant candidate functions of each model are selected and a model inference step where the coefficients of the models are obtained.

Model Discovery

Once the corrective fields R and b_{ij}^{Δ} are obtained and the library of available functions has been defined, the learning process can start. The technique here is the Sparse Regression of Turbulent stress anisotropy (SpaRTA) first introduced by Schmelzer et al. [38]. In order for the models to be interpretable and stable when implemented into the CFD solver and to avoid over fitting, it is desirable to find a solution with only a few terms and with small coefficients. These properties are satisfied by searching the space of solution thanks to an elastic net as:

$$\Theta = \underset{\Theta}{\mathrm{argmin}} ||C\Theta - \Delta||_2^2 + \lambda\rho||\Theta||_1 + 0.5\lambda(1-\rho)||\Theta||_2^2 \tag{3.22}$$

With Δ the target (either R or P_k^{Δ}), C the library functions and Θ the coefficients, ρ the mixing parameter and λ the regularization weight. Here, the candidates and targets are standardized . The l_1 norm in the second term favors sparse models and lets only a few non-zero coefficients when the l_2 one in the third term favors small coefficients in the solution. The balance between the terms is made by adjusting the mixing parameter and regularization weight. The data are separated randomly into a training and a testing set. The solutions found by applying the elastic net on the training set are only kept if they show good performance on the testing set. The mixing parameter is set to :

$$\rho = [0.01, 0.1, 0.2, 0.5, 0.7, 0.9, 0.95, 0.99, 1.0] \tag{3.23}$$

The regularization weight is chosen in a vector of 100 entries spaced in a logarithmic way between $10^{-3}\lambda_{max}$ and λ_{max} with $\lambda_{max} = max(|C_{\Delta}^{T}\Delta|)/(K\rho)$ and K is the number of points.

Model Inference

The model discovery step used standardized functions. In order to find the correct coefficients for the models a model inference step is performed on real value functions. Non-relevant functions have already been eliminated by setting their coefficient to zero in the previous step. It is thus not necessary to promote sparsity at this step and only a l_2 is used to promote small coefficients. The model coefficients are thus found following:

$$\Theta = \underset{\Theta}{\operatorname{argmin}} ||C\Theta - \Delta||_2^2 + \lambda_r ||\Theta||_2^2 \tag{3.24}$$

With λ_r the Tikhonov-regularisation parameter. This parameter is set to 0.01, 0.05 and 0.1 in this study.

3.2.6. Error metrics

The evaluation of the error introduced by the models is done by comparing the true value of R or P_k^Δ with the one given by the models. Due to the high values of these target data in the boundary layer where models are discovered, the error metric is chosen to be the normalized root mean square expressed as:

$$e = \frac{1/N\sqrt{\sum^{N}(\Delta - \Delta model)^2}}{max(\Delta)} \tag{3.25}$$

Some profiles at relevant points of interest in the region before the wing, the separation region, the vortex system and the wake are exhibited for visualization and a more precise analysis of the errors.

4

LES Results

In this chapter, the results of the wall-resolved LES are analyzed. The LES approach taken here has been validated by Alberts [2] by comparing the baseline case to the experimental results of Devenport and Simpson [9] and Ölçmen and Simpson [49]. Thus, the main focus will be on providing a comparison between the LES of the baseline case of the body wing junction and the Anti-Fairing case.

4.1. Boundary layer profiles

In Figure 4.1, a comparison is made between the streamwise velocity profile in the symmetry plane (Z = 0) for the baseline and Anti-Fairing case.

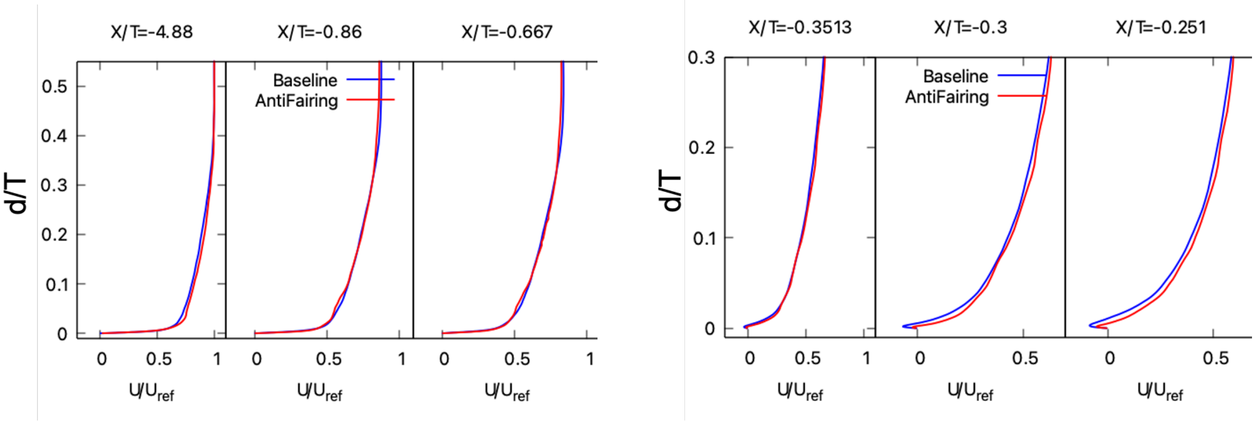

Figure 4.1: Streamwise velocity profile in the boundary layer at $Z = 0$

The y-axis corresponds to the distance to the bottom wall in order to also compare the two cases in the region of dent and is normalized by the wing thickness T. The velocity is normalized by the freestream value U_{ref}. In both cases, the streamwise velocity U is decreasing in the boundary layer due to the adverse pressure gradient until separation. Before separation, the profiles of the two cases are very similar although the velocity in the top part of the boundary layer is lower in the case of the Anti-Fairing. The separation region is less important for the Anti-Fairing case.

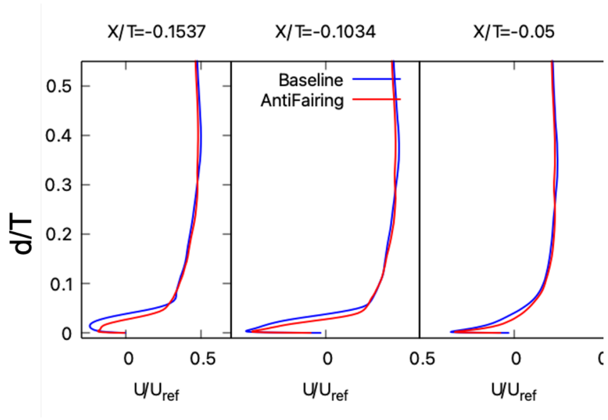

Figure 4.1: Streamwise velocity profile in the boundary layer at $Z = 0$ (cont.)

4.2. Surface quantities

4.2.1. Mean pressure coefficient on the bottom wall

The pressure coefficient C_p is expressed as :

$$C_p = \frac{P - P_\infty}{0.5\rho U_{ref}^2} \tag{4.1}$$

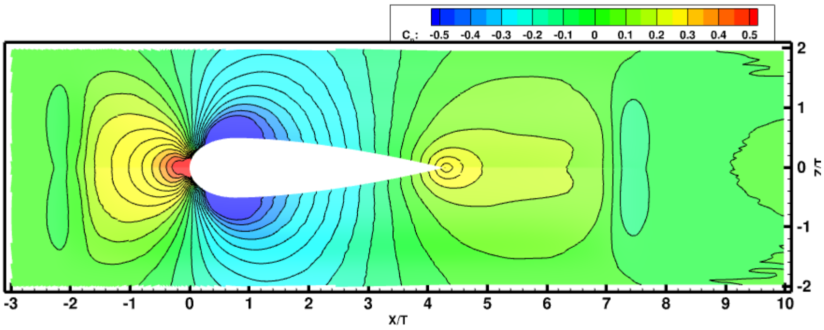

Figure 4.2: Pressure coefficient on the wall surface for the AntiFairing case

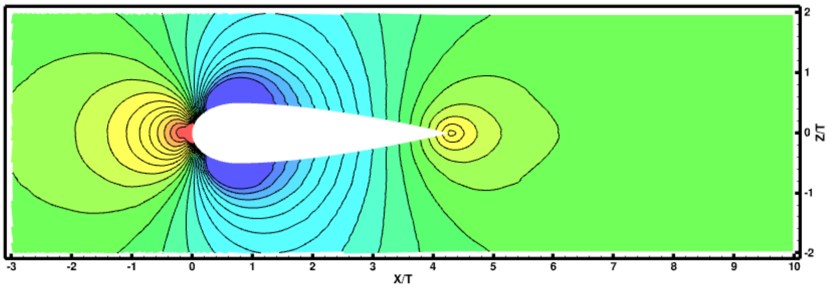

Figure 4.3: Pressure coefficient on the wall surface for the baseline case from Alberts [2]

Visualizations of the pressure coefficients are shown in Figure 4.2 and Figure 4.3. In the baseline and Anti-Fairing cases, the pressure increases as the flow upstream of the wing gets closer to the obstacle. The pressure raises to higher values at the nose of the wing in the case of the Anti-Fairing. This is confirmed by Figure 4.4 where it is possible to see that the region where $C_p > 0.2$ starts at

$X/T = -1.3$ compared to $X/T = -1.1$ in baseline case. A similar observation was made by Kumar [23] in his wall-modeled LES simulation of the same configurations.

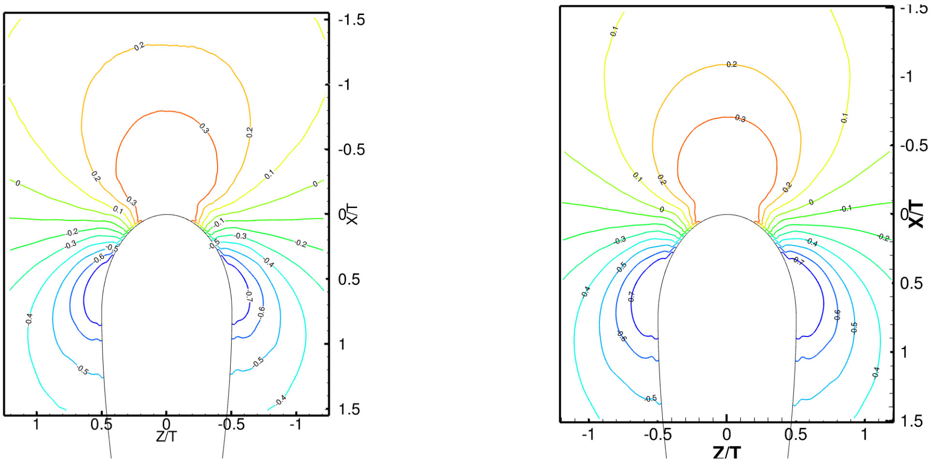

(a) AntiFairing case

(b) Baseline case from Alberts [2]

Figure 4.4: Pressure coefficient on the wall surface near the wing

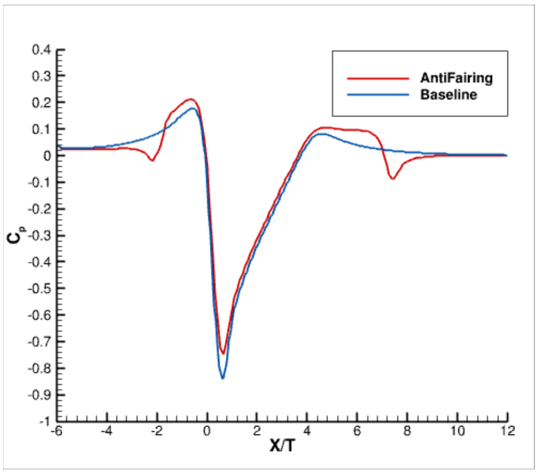

Figure 4.5: Pressure coefficient C_p at $Z/T = -0.6$

As can be seen in Figure 4.2 , the dent of the Anti-Fairing junction greatly affects the pressure field. This effect is illustrated more precisely in Figure 4.5 where the wall pressure coefficient is plotted along a line located at $Z/T = -0.6$.

Upstream of the Anti-Fairing dent, the pressure is constant while it raises slowly in the baseline case. At the dent, around $X/T = -2.1$, the pressure coefficient becomes negative before experiencing a fast increase and becoming higher than the one of the baseline case. This is due to the conjugate effects of the obstacle and the concavity of the bottom wall.

A similar pattern is observed at the trailing edge of the wing. In the baseline case, the pressure recovers smoothly, while in the Anti-fairing case it plateaus before dropping at $X/T = 7.5$ where the dent ends and finally recovering.

Along the wing, the flow is accelerated up to the point of maximum thickness and is slowed down afterwards. This translates into a fast decrease and then an increase of the pressure coefficient.

Figure 4.5 shows a minimum pressure coefficient of $C_p = -0.72$ for the Anti-Fairing and $C_p = -0.84$ for the baseline case, both values are lower than the one predicted in the previous study of Kumar [23] respectively $C_p = -0.65$ and $C_p = -0.62$.

4.2.2. Streamlines on the bottom wall

Figure 4.6a shows the streamlines on the bottom wall for the baseline and Anti-Fairing configurations. The top plot corresponds to the baseline and the bottom one to the Anti-Fairing case. Two separation lines are present. The first separation line starts upstream of the wing at the point of separation located around $X/T = -0.5$ and continues around both sides of the wing. The second line of separation starts around $X/T = -0.025$. A third separation line, very close to the wing, is also present although less visible here. The locations of the first separation point are different in the baseline and Anti-fairing case: the separation line is located closer to the wing in the case of the Anti-Fairing. This is in agreement with the observation made by Belligoli et al. [6] when using the Spalart– Allmaras (S-A) RANS turbulence model, reproduced in Figure 4.6b. The $y-axis$ in Belligoli et al. [6] corresponds to the present $z-axis$.

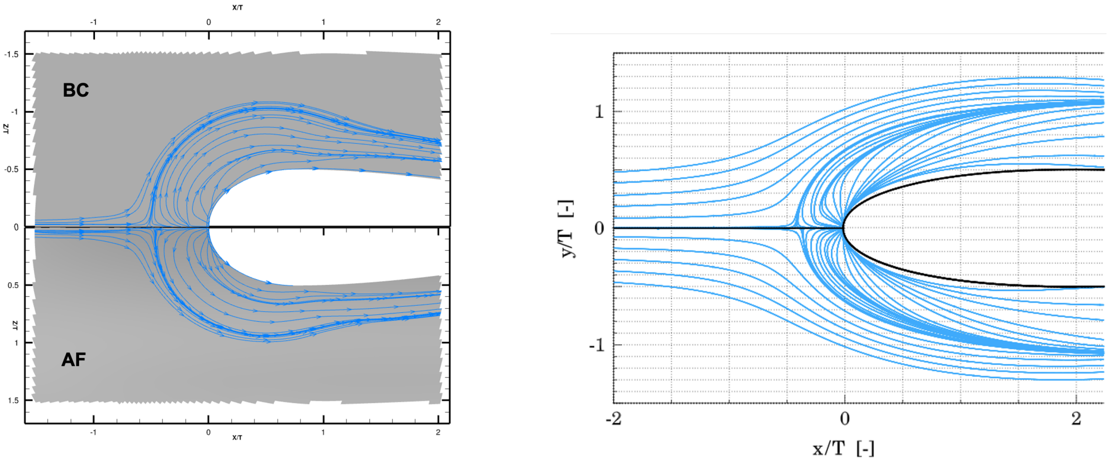

(a) Streamlines on the bottom wall upstream of the wing - Wall-resolved LES

(b) Streamlines on the bottom wall upstream of the wing from S-A RANS from Belligoli et al. [6]

Figure 4.6: Streamlines on the bottom wall

4.3. Symmetry plane

In this section, the variables of interest for the two simulations are compared at the plane of symmetry ($Z = 0$) in the vicinity of the leading edge of the wing.

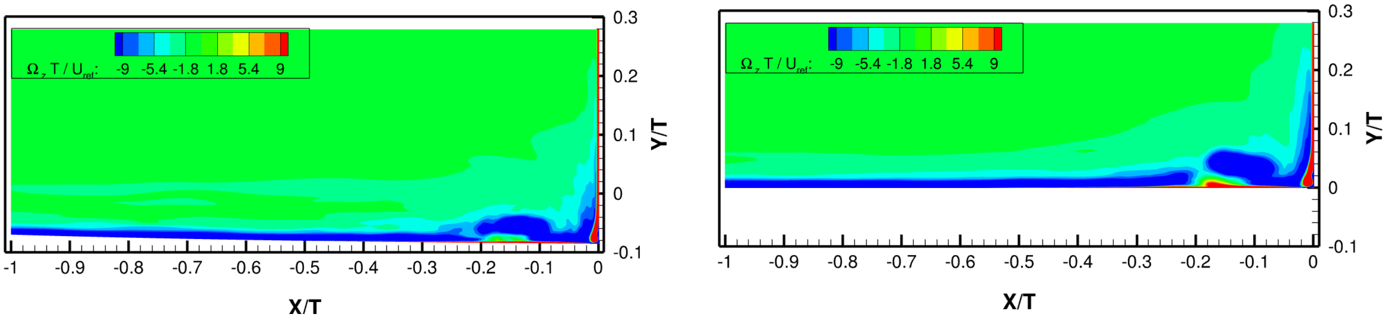

(a) Anti-Fairing - Present study

(b) Baseline case from Alberts [2]

Figure 4.7: Vorticity in the symmetry plane

The spanwise time-averaged vorticity Ω_z is represented in Figure 4.7. It is normalized by the wing thickness and the reference velocity. Both cases show an elliptic lump of negative vorticity raising above a region of positive vorticity located close to the wall. In addition, a tong of negative vorticity attached to the wall starting from upstream is present. Junctions flows are characterized by an aperiodic shift between a backflow mode with negative velocity and a zero flow mode. The interaction between the backflow mode and the zero flow creates the ejection of the flow in the upstream direction which explains why the negative vorticity is slightly lifted. In the case of the Anti-Fairing the positive vorticity is considerably smaller than in the baseline case and the two regions of negative vorticity appear to be closer in the mean visualization. In addition, the vortex is closer to the bottom wall.

In the corner, a secondary vortex of positive vorticity can be observed in both cases. It is the result of the flow encountering the wing and going downwards. This secondary vortex has a reduced size in the Anti-Fairing case compared to the baseline case.

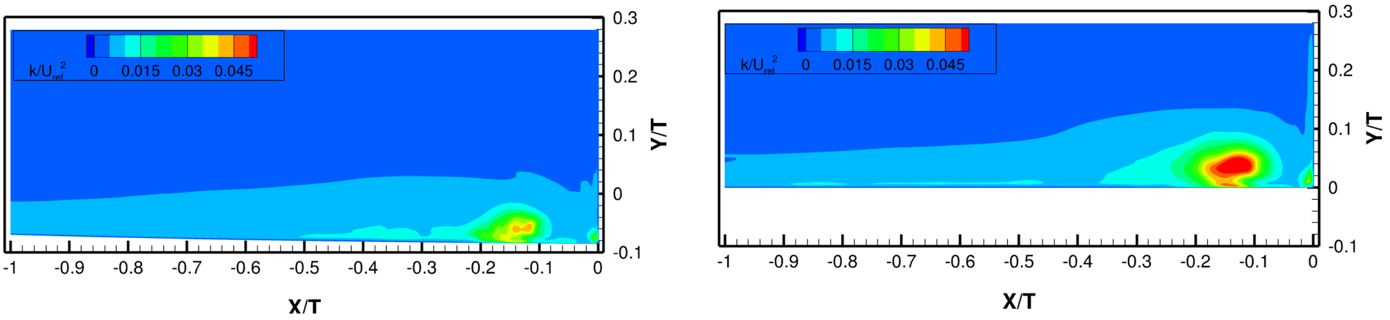

(a) Anti-Fairing - Present study

(b) Baseline case from Alberts [2]

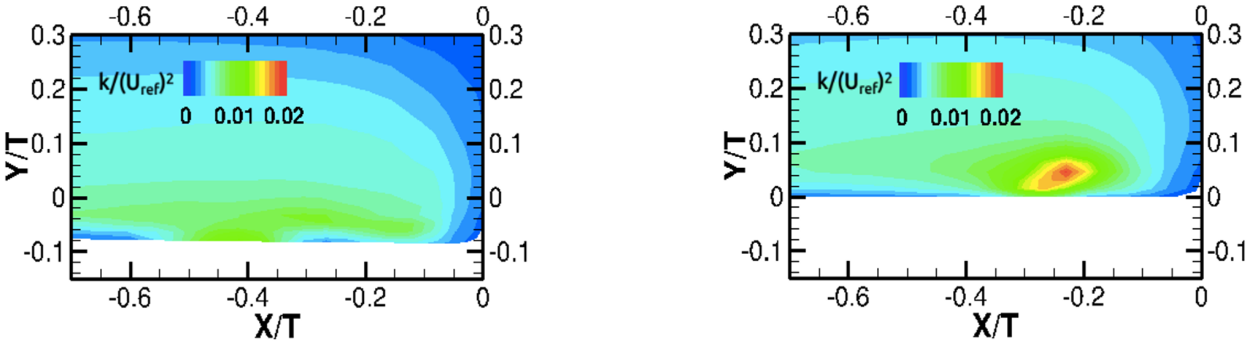

(c) Anti-Fairing - from Kumar [23]

(d) Baseline case from Kumar [23]

Figure 4.8: Turbulent kinetic energy in the symmetry plane

Figure 4.8 shows contours for the normalized turbulent kinetic energy in the plane of symmetry. Both the Anti-Fairing and the baseline cases present a region of high time-averaged t.k.e having a C shape made of two peaks. The first peak is located near the wall and the second peak is located approximately at the location of the time-averaged main vortex. The C shape is a characteristic feature of body-junction flows reported in the experiment of Devenport and Simpson [9] and in the DES of Paik et al. [33] and the LES of Ryu et al. [37]. In both cases, a secondary peak of t.k.e associated with the corner vortex is present. Its intensity is slightly lower than the one of the main vortex.

In the case of the Anti-Fairing, the size of the pocket of high t.k.e is smaller compared to the baseline case and the vortex is located closer to the wall. The maximum t.k.e in the Anti-Fairing case is about

33% lower than the one in the baseline case equal to $k/U_{ref}^2 = 0.064$. This is close to the 40% found by Kumar [23] in his wall modeled LES reproduced in Figure 4.8c and Figure 4.8d. It is to be noted though that the wall modeled LES fails at representing the correct shape for the turbulent kinetic energy in the Anti-Fairing case. In Figure 4.8, it is difficult to assess a difference in the distance to the wing between the Anti-Fairing and the baseline case, despite the fact that separation occurs later in the Anti-Fairing case.

The decrease in turbulent kinetic energy in the Anti-Fairing case can be linked to the convex surface of the dent. Indeed, authors such as Muck et al. [29] point out the stabilization nature of convex walls which tend to decrease the turbulence in the boundary layer. In order to see the impact of the Anti-Fairing on the turbulent kinetic energy more precisely, some profiles are reproduced in Figure 4.9. Downstream of the start of the dent and upstream of separation, the turbulent kinetic energy profiles already differ between the two cases. The peak of the maximum kinetic energy of the upstream boundary layer in the Anti-Fairing case is lower. In the vortex region, this translates in a double peak of energy with a lower maximum value and with a smaller extent as could be seen in the contour plots.

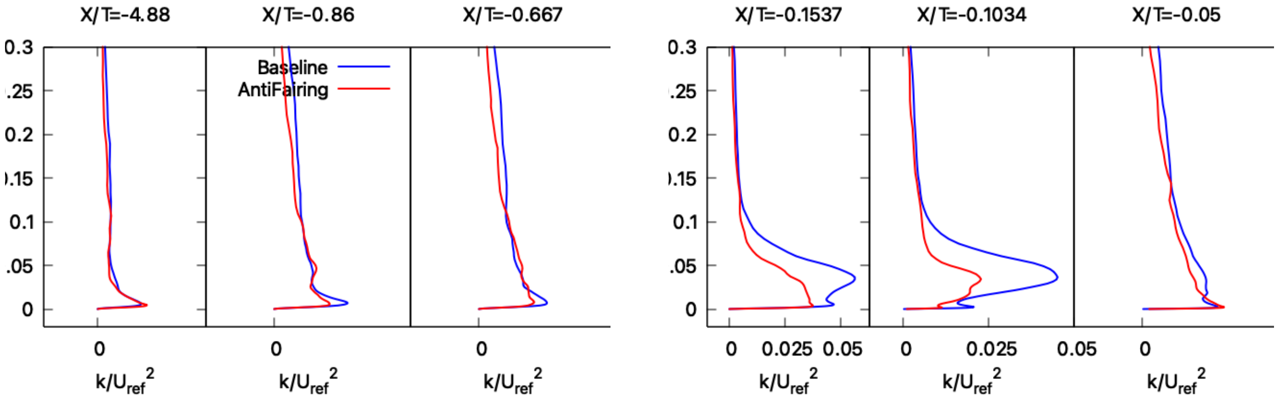

Figure 4.9: Comparison of turbulent kinetic energy in the symmetry plane

4.4. Bimodal behavior

The shift between the backflow mode and the zero flow mode can be further investigated by plotting the probability density function (PDF) of the stream wise component of the velocity.

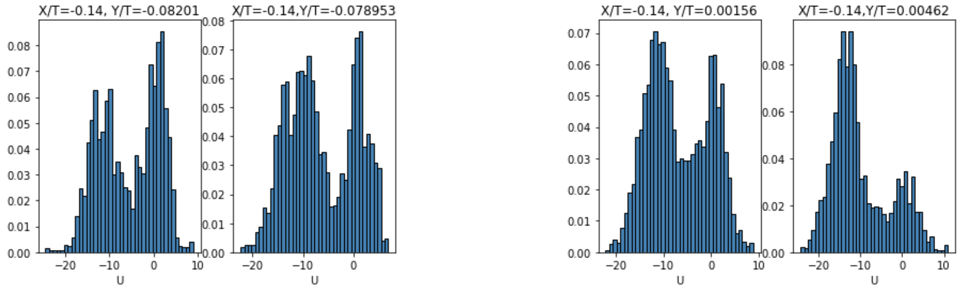

(a) AntiFairing case

(b) Baseline case from Alberts [2]

Figure 4.10: PDF of the velocity for baseline and AntiFairing case

Figure 4.10 shows the PDF of U for the baseline and Anti-Fairing case at $X/T = -0.14$, and $Z/T = 0$ for four locations upstream of the wall. The signal is taken at the same distance from the wall in both cases. The Anti-Fairing case presents two peaks in the vortex region in the first two stations close

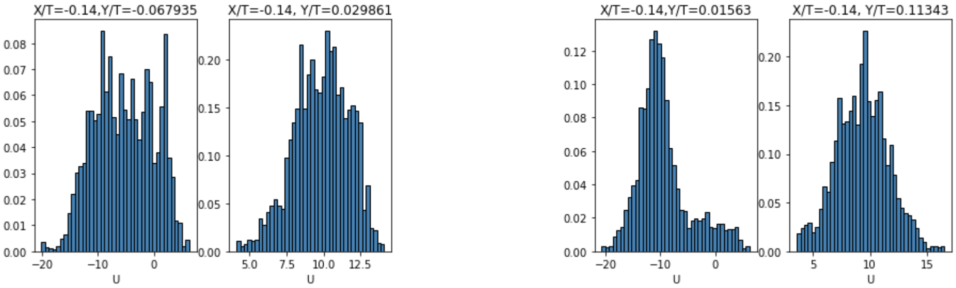

(c) AntiFairing case

(d) Baseline case from Alberts [2]

Figure 4.10: PDF of the velocity for baseline and AntiFairing case (cont.)

to the wall. The first peak happens at negative velocity and corresponds to the backflow mode and the second peak happens at a velocity close to zero and corresponds to the zero flow mode. This is an indication that the Anti-Fairing does not alter the bimodal behavior of the vortex. Contrary to the baseline case where the third location shows the mark of the zero flow mode, the Anti-Fairing presents a single peak of negative velocity. This is consistent with the reduced size of the vortex shown in Figure 4.7a.

4.5. Flow quantities around the wing and in the wake

In this section, the velocity and streamwise vorticity around the wing and in the wake are compared between the Anti-fairing and the baseline case. The planes located at the beginning of the wing $X/T = 0$ and the end of the wing $X/T = 4.2$ and two additional planes in-between at $X/T = 1.4$ and $X/T = 2.8$ are selected. In the wake, a plane at $X/T = 5.33$ and $X/T = 10$ are selected.

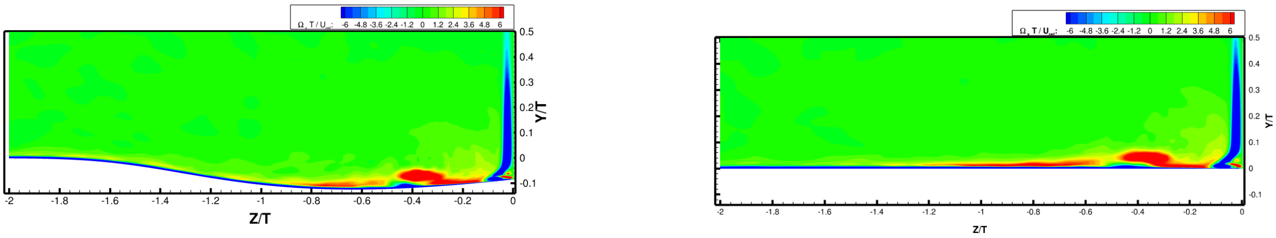

(a) Anti-Fairing at $X/T = 0$ - Present study

(b) Baseline case at $X/T = 0$ from Alberts [2]

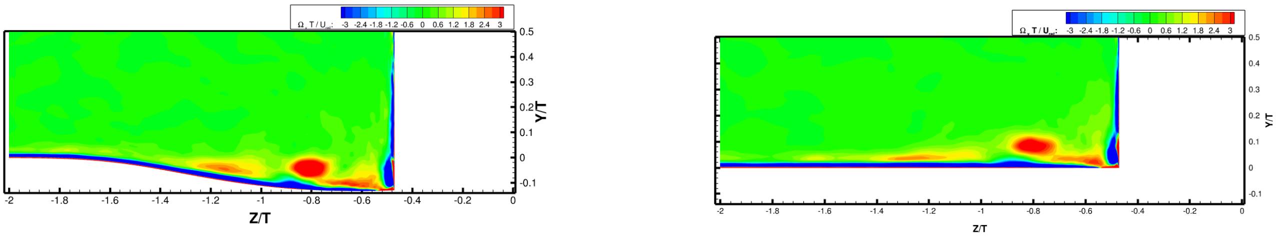

(c) Anti-Fairing at $X/T = 1.4$ - Present study

(d) Baseline case at $X/T = 1.4$ from Alberts [2]

Figure 4.11: Streamwise vorticity at $X/T = 0$ and $X/T = 1.4$

Figure 4.11 and Figure 4.12 display the streamwise vorticity along the wing. For both cases, the main horseshoe vortex and the corner vortex are clearly visible. The main horseshoe vortex is initially elliptic with a shape very similar to the one in the symmetry plane. When traveling along the wing, its shape becomes rounder and raises above the surface. Its strength also decreases in both cases. Finally, at $X/T = 4.2$, the vortex shape is a lot more diffuse.

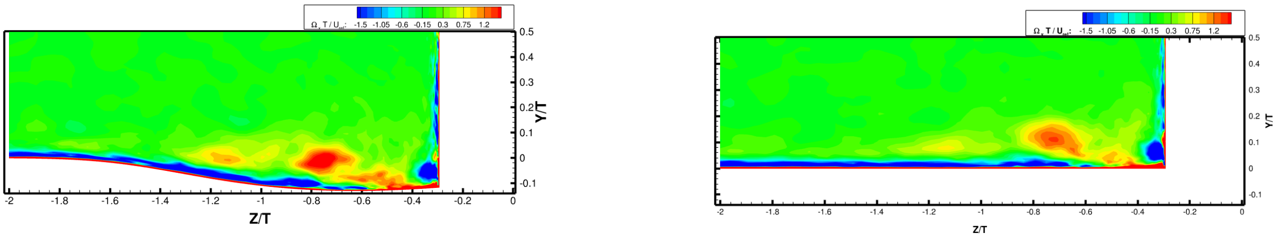

(a) Anti-Fairing at $X/T = 2.8$ - Present study

(b) Baseline case at $X/T = 2.8$ from Alberts [2]

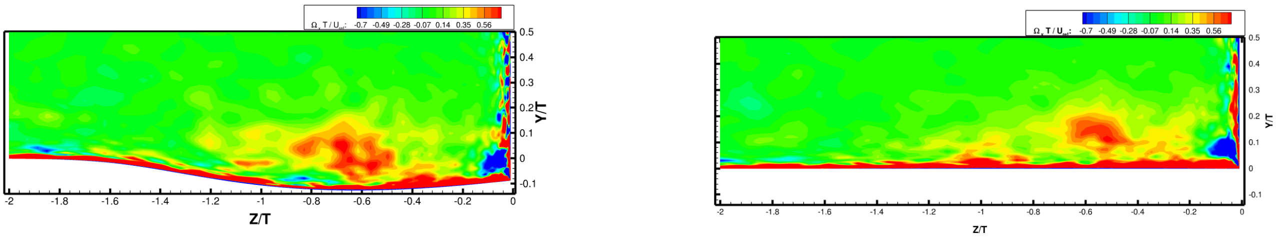

(c) Anti-Fairing at $X/T = 4.2$ - Present study

(d) Baseline case at $X/T = 4.2$ from Alberts [2]

Figure 4.12: Streamwise vorticity $X/T = 2.8$ and $X/T = 4.2$

In the Anti-Fairing case, the vortex seems to be located slightly further from the wing than in the baseline case. For example at $X/T = 2.8$ the vortex is located at $Z/T = -0.76$ in the Anti-Fairing case and $Z/T = -0.72$ in the baseline case. This effect is less visible than in the results of Kumar [23]. Vorticity in the wake will be plotted to see if the trend is similar past the wing.

When comparing Figure 4.11d and Figure 4.12b to the wall modeled LES of Kumar [23] shown in Figure 4.13a and Figure 4.13b, it is possible to see that the predicted locations of the main vortex follow different trends. Wall modeled LES predicts the location of the main vortex to be $Z/T = 1.15$ at $X/T = 1.4$ and $Z/T = 1.3$ at $X/T = 2.8$ while wall resolved LES predicts it to be respectively at $Z/T = 0.8$ and $Z/T = 0.72$. Both the distance from the wing in a given plane and the evolution of the vortex when moving downstream along the wing are different: Kumar [23] predicts a vortex far from the wing that is pushed further when convected when Alberts [2] and the present study show vortices close to the wall and which locations follow more the curve of the wing.

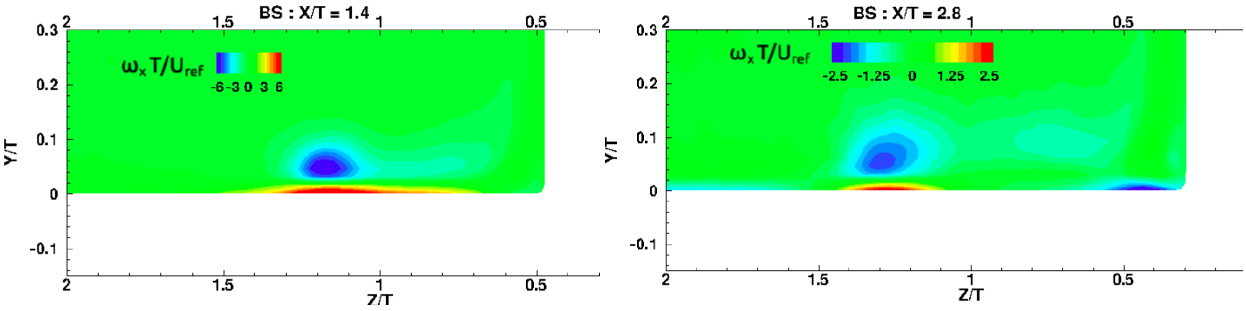

(a) Baseline case at $X/T = 1.4$ from Kumar [23]

(b) Baseline case at $X/T = 2.8$ from Kumar [23]

Figure 4.13: Streamwise vorticity in baseline case from Kumar [23]

The velocity is also plotted at the $X/T = 1.4$ and $X/T = 4.2$ in Figure 4.14 to see the influence of the vortex on the mean velocity.

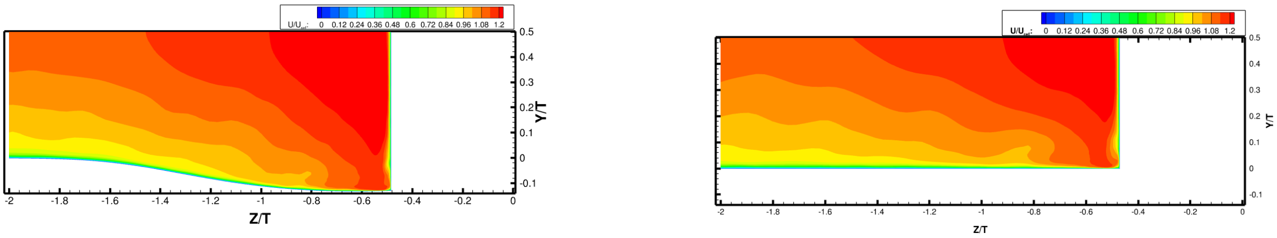

(a) Anti-Fairing at $X/T = 1.4$- Present study

(b) Baseline case at $X/T = 1.4$ from Alberts [2]

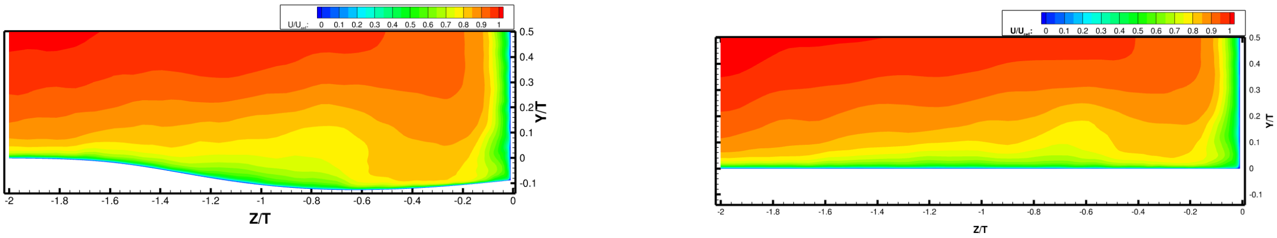

(c) Anti-Fairing at $X/T = 4.2$ - Present study

(d) Baseline case at $X/T = 4.2$ from Alberts [2]

Figure 4.14: Streamwise velocity at $X/T = 1.4$ and $X/T = 4.2$

The velocity plots exhibit a bump located close to the location of the vortex. In Figure 4.14d and Figure 4.14c, it is possible to see that the size of the bump at $X/T = 4.2$ is more important in the Anti-Fairing case than in the baseline case. The velocity in the other two planes as well as the turbulent kinetic energy can be seen in Appendix A.

In the wake, the vorticity is represented in Figure 4.15. The trend is similar to the one observed close to the wing trailing edge. The vorticity has a diffuse pattern that flattens when being convected downstream. The impact on the velocity is represented in Figure 4.16. It can be seen that from the station located at $X/T = 5.33$ and the one located at $X/T = 10$ the increase in velocity has been pushed away from the symmetry plane. Similarly to the experiment of Belligoli et al. [6], at $X/T = 5.33$ the velocity shows that the vortex is further away from the wing in the Anti-Fairing case compared to the baseline case. The effect is even more visible at $X/T = 10$.

In the Anti-Fairing case, from the velocity, vorticity and turbulent kinetic energy plots, it was observed that in the symmetry plane the separation is weaker and happening later , that the main horseshoe vortex core is closer to the bottom wall, and that the distance between the legs of the vortices is increased. In Belligoli et al. [6] it was observed experimentally that in the case of the Anti-Fairing, the distance between the two legs of the horseshoe vortex is increased. In addition, using Spalart-Allmaras model delayed separation was observed for the Anti-Fairing. Fleming et al. [14] introduced the momentum deficit factor (MDF) to quantify the impact of the incoming boundary layer on the horseshoe vortex. High MDF has been linked to increased distance between the leg of the vortex, a vortex closer to the wall and closer to the wing. This wall-resolved LES confirms the hypothesis of Belligoli et al. [6] and Kumar [23] about the role of the high MDF in the case of the Anti-Fairing configuration.

As for the decreased turbulence intensity, it can be attributed to the convex nature of the dent.

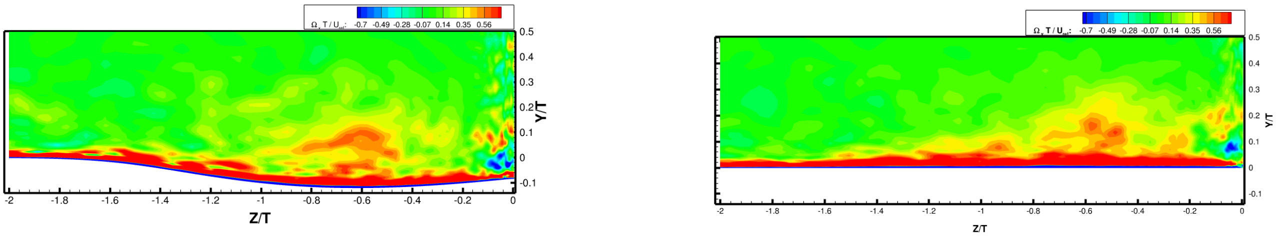

(a) Anti-Fairing at $X/T = 5.33$ - Present study

(b) Baseline case at $X/T = 5.33$ from Alberts [2]

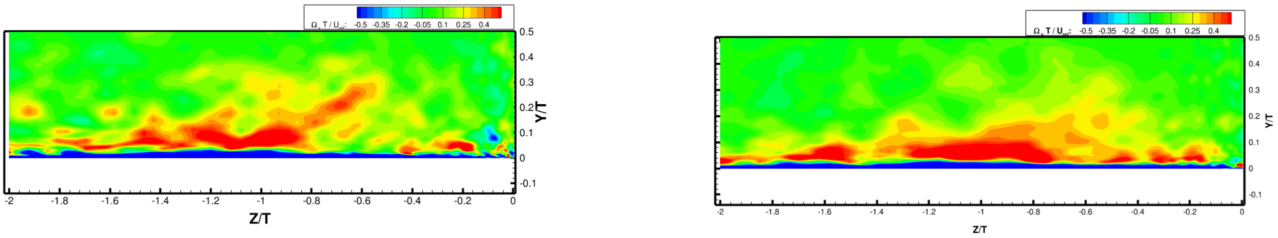

(c) Anti-Fairing at $X/T = 10$ - Present study

(d) Baseline case at $X/T = 1.4$ from Alberts [2]

Figure 4.15: Streamwise vorticity in the wake

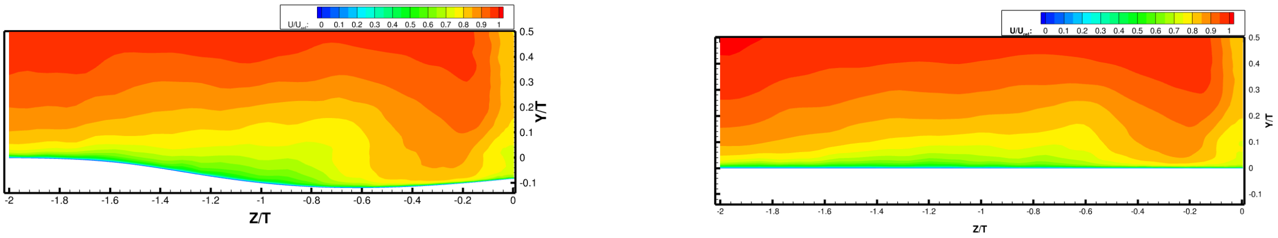

(a) Anti-Fairing at $X/T = 5.33$- Present study

(b) Baseline case at $X/T = 5.33$ from Alberts [2]

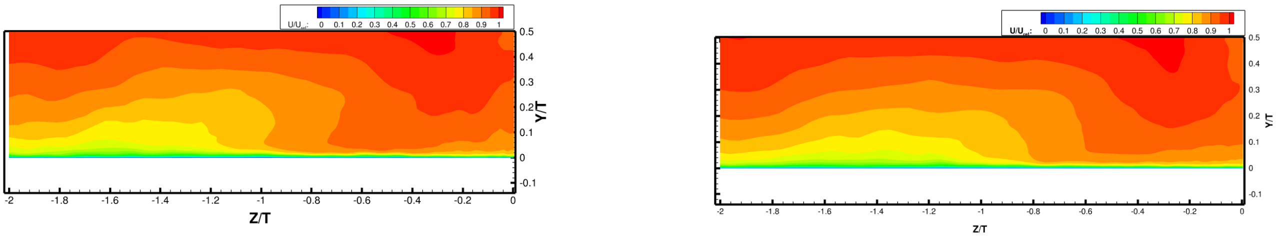

(c) Anti-Fairing at $X/T = 10$ - Present study

(d) Baseline case at $X/T = 10$ from Alberts [2]

Figure 4.16: Streamwise velocity in the wake

5

Data driven turbulence modeling

In this chapter, the results at the different steps of the SpaRTA methodology are presented. The first step constitutes the k-corrective frozen approach. It is followed by the results of the Mutual Information calculation and the determination of the relevant functions for the library. Then the outputs of the SpaRTA algorithm itself are presented.

5.1. k-corrective frozen RANS

In the k-corrective frozen RANS step, two corrective terms for the RANS equations are obtained. First, selected profiles and contours plots showing these two terms are displayed. These plots will be the base for a discussion on the selection of the training data and also provide additional information on where the RANS models fail to represent accurately the body-wing junction. Secondly, the result of the addition of these terms in a RANS simulation is shown in order to verify the performance of these target data. The results obtained at this step are expected to be the maximum performance that can later reach the SpaRTA models.

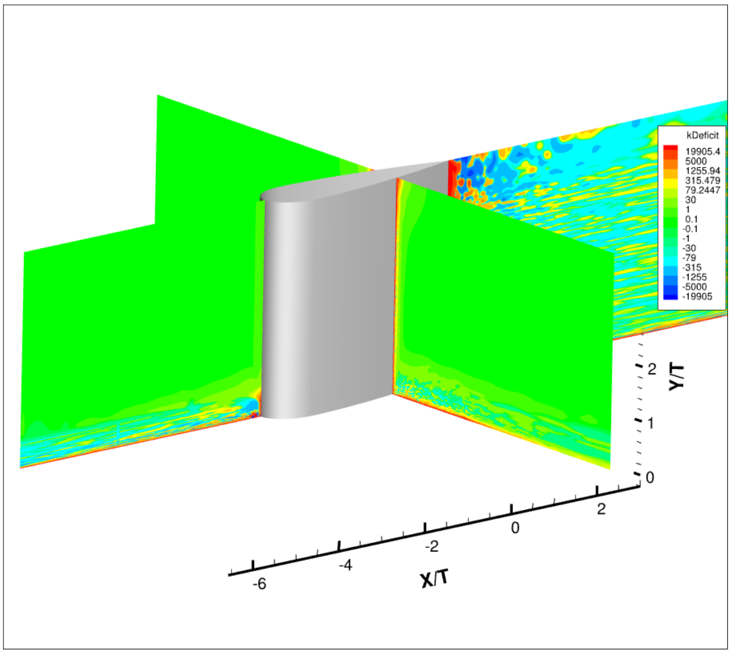

Figure 5.1: Overview of the turbulent kinetic energy deficit R

Figure 5.1 shows an overview of the deficit in turbulent kinetic energy in the domain. Two planes are represented : the symmetry plane at $Z = 0$ and a plane along the wing located at $X/T = 2.8$. As expected, the deficit is concentrated in the boundary layer around the wing and the flat plate. The noisy deficit downstream of the wing at $Z = 0$ is disappearing when looking away from the symmetry plane. These observations confirm that the training data can be taken in the boundary layer only.

Figure 5.2a displays a closer view of R in the symmetry plane in the boundary layer, upstream of the wing. The corrective action of R is apparent here: a strong positive deficit is located at the location of the C shape vortex while strong negative values are surrounding it. A similar phenomenon can be seen in the corner vortex region. The turbulent kinetic energy deficit is forcing the RANS simulation to adopt the right shape for the two vortices.
Also apparent in Figure 5.2a is a correction in the near-wall boundary layer. This correction is also present in the boundary layer around the wing as can be seen in Figure 5.4b. The RANS simulations seem to have an incorrect boundary layer profile at small $y+$. Figure 5.5 is shown to quantify further this effect.

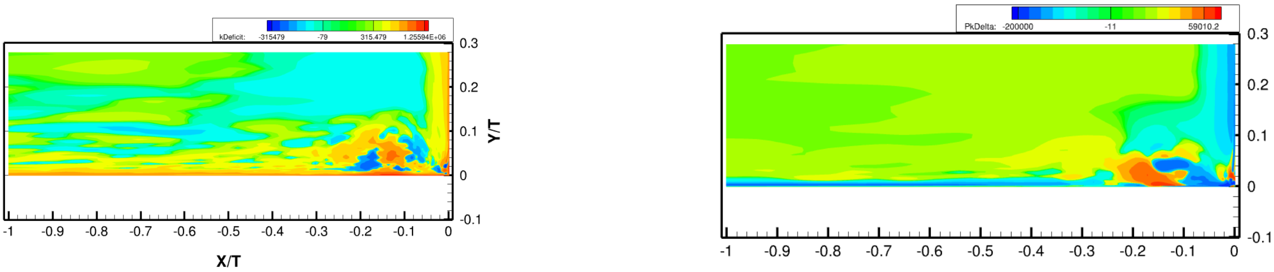

(a) Turbulent kinetic energy deficit R at $Z = 0$

(b) P_k^Δ at $Z = 0$

Figure 5.2: Corrective fields in the symmetry plane

Figure 5.2b displays $P_k^\Delta = -2kb_{ij}^\Delta \frac{\partial U_i}{\partial U_j}$. The strongest corrections introduced by P_k^Δ are also in the vortex region and the inner part of the incoming boundary layer. Both the positive and negative lumps in the vortex area are aligned with the direction of the base of the C-Shape vortex.
In the inner part of the upstream boundary layer, the values are negative which is in opposition to what was observed for R.
To see the complete impact of the two corrections to the production of turbulent kinetic energy, the sum of R and P_k^Δ is shown in Figure 5.3 .

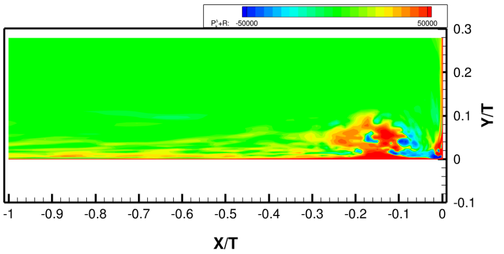

Figure 5.3: $P_k^\Delta + R$ at $Z = 0$

The strong variations of the turbulent kinetic energy are dampened when looking downstream along the wing as can be seen by comparing the turbulent kinetic energy deficit at $X = 0$ in Figure 5.4a and at $X/T = 1.4$ in Figure 5.4b. This is coherent with the decreasing strength of the turbulent kinetic energy downstream.

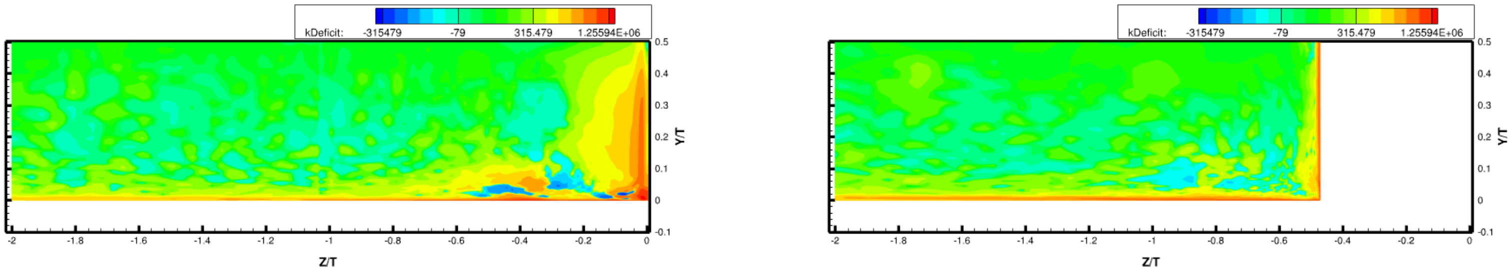

(a) Turbulent kinetic energy deficit R at $X = 0$

(b) Turbulent kinetic energy deficit R at $X = 1.4$

Figure 5.4: Corrective fields along the wing

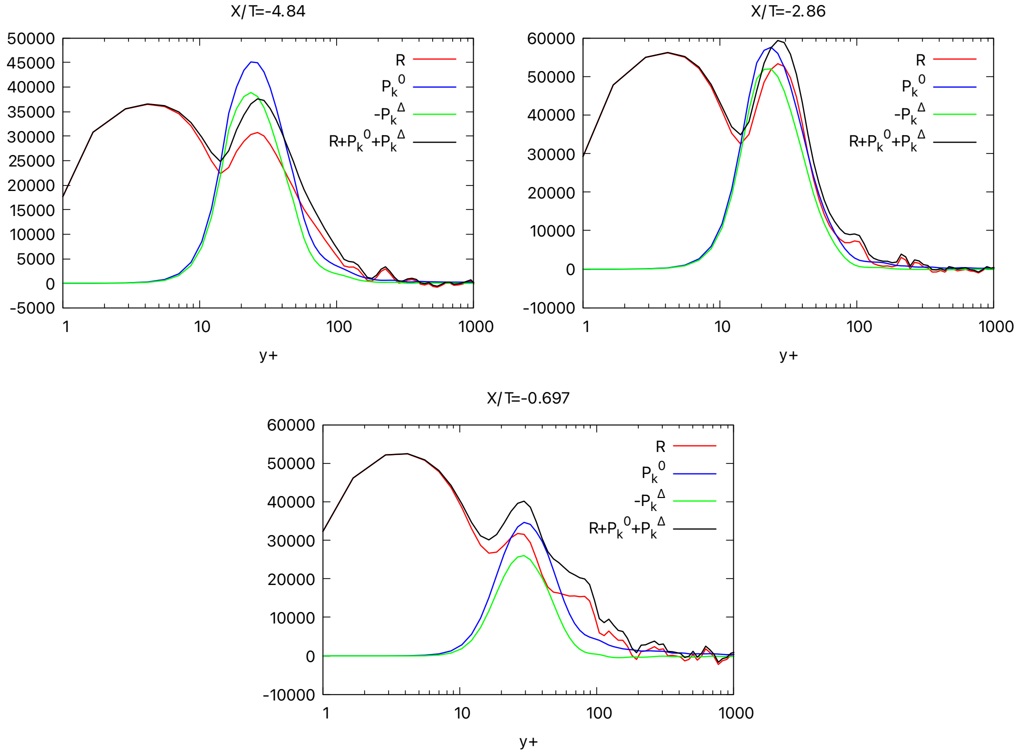

Figure 5.5: Turbulent kinetic energy deficit R, P_k^Δ and Boussinesq production of energy profiles at $Z/T = 0$

In Figure 5.5 the turbulent kinetic energy deficit profiles at different locations upstream of the wing are plotted to better understand the correction shown in Figure 5.2a. In the near wall boundary layer R is composed of two peaks: one below $y+ \approx 12$ and one above it. The second peak location corresponds roughly to the one of the peak in the Boussinesq production of turbulent kinetic energy. Their magnitudes are similar. The first one doesn't have any equivalent. In the following, it is decided that the data below $y+ \approx 14$ will not be kept for the training. Indeed, our features being normalized by ω, reaching the first peak would likely require large coefficients for the models without important gains in the predicted fields.

Figure 5.5 also reveals that P_k^Δ has a shape very similar to the Boussinesq production of energy although its magnitude and sign are different. This behavior is not occurring in the vicinity of the vortex where the Boussinesq production and P_k^Δ are very different as can be seen in Figure 5.6.

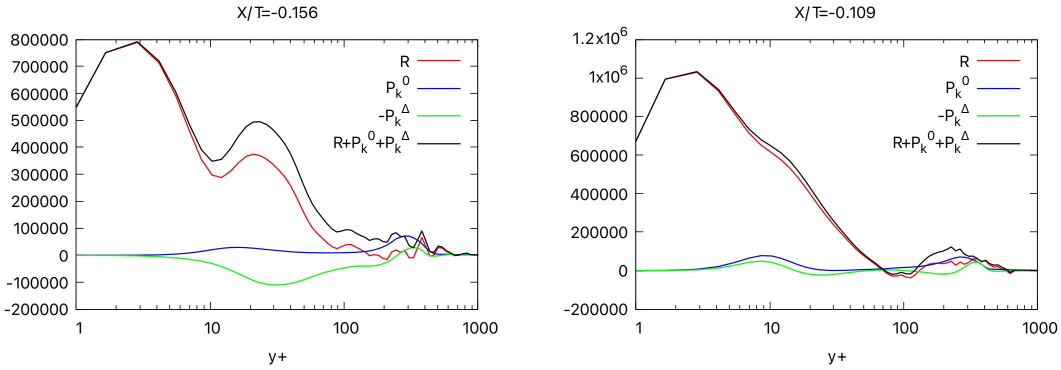

Figure 5.6: Turbulent kinetic energy deficit R, P_k^{Δ} and Boussinesq production of energy profiles at $Z/T = 0$ close to the vortex

To validate the k-corrective frozen approach, the corrective fields R and b_{ij}^{Δ} are added to a $k-\omega\ SST$ model and a propagation step is performed. The results on the turbulent kinetic energy are shown in Figure 5.7 and compared to the LES results. Overall there is an excellent agreement between the turbulent kinetic energy obtained by propagating the frozen fields and the LES results. The location, magnitude and size of the main horseshoe vortex are well captured. The corner vortex shape is slightly mispredicted. In the training data, the region located at a distance below 0.65 from the wing will not be used.

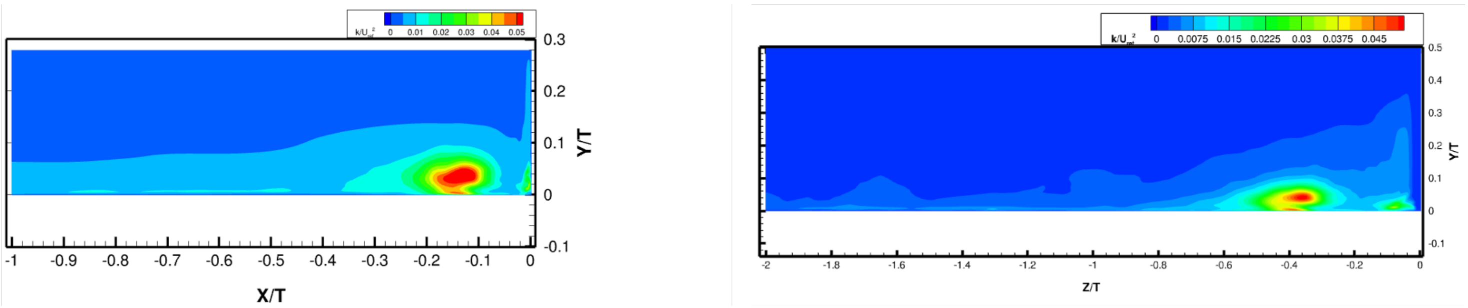

(a) Propagation of corrective fields - Plane of symmetry view

(b) Propagation of corrective fields - Side view at $X = 0$

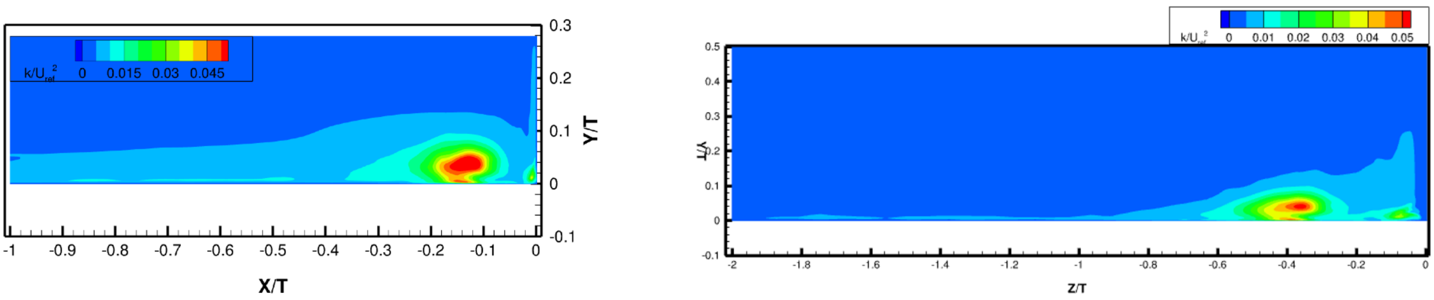

(c) LES - Plane of symmetry view

(d) LES - Side view at $X = 0$

Figure 5.7: Turbulent kinetic energy obtained from propagation of the frozen fields

As models were difficult to find for b_{ij}^{Δ}, it is interesting to look at the result of propagating only P_k^{Δ} and R. Figure 5.8 shows a real lack of accuracy when the correction to the Reynolds stress tensor is not implemented. The turbulent kinetic energy is indeed raised inside the vortex but is now overpredicted compared to the LES. The C-shape of the vortex is only roughly captured and the corner vortex appears to be deformed too. The location of the vortex is improved compared to RANS models but is not as accurate as when both R and b_{ij}^{Δ} are propagated.

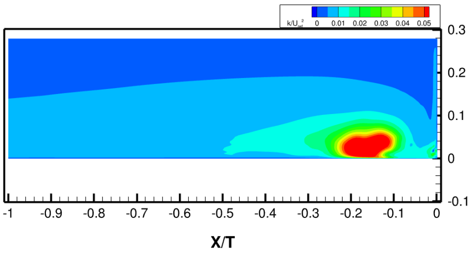

Figure 5.8: Propagation of $P_k^{\Delta} + R$ at $Z = 0$

5.2. Feature selections

The invariants, tensors and physical features used to build the library can be selected among the lists in Equation 3.15, Equation 3.14 and Table 3.1. Creating the library using all of these features and following the method described in subsection 3.2.3 would result in a very high number of models in the library. The results from the calculation of Mutual Information are shown and the relevant features are selected based on it. The mutual information in two regions of the flow described in Section 3.2.2 are compared. For simplicity, the first region including part of the incoming flow before any separation of creation of vortices is called the upstream region in this section, and the second region surrounding the beginning of the vortex is called the vortex region. As explained in the previous section, values having $y+ < 14$, being outside of the boundary layer and being too close to the wing are also excluded in these regions.

5.2.1. Tensors

Mutual information is first employed to determined the dependency of R and P_k^{Δ} on the tensors. The resulting histograms are shown in Figure 5.9b for R, Figure 5.10b for b_{ij}^{Δ} and Figure 5.11 for P_k^{Δ}. The mutual information for R and P_k^{Δ} is actually taken between the corrective term and the inner product of the tensor with the gradient of the velocity $T_{ij}^{(n)} \frac{\partial U_i}{\partial x_j}$.

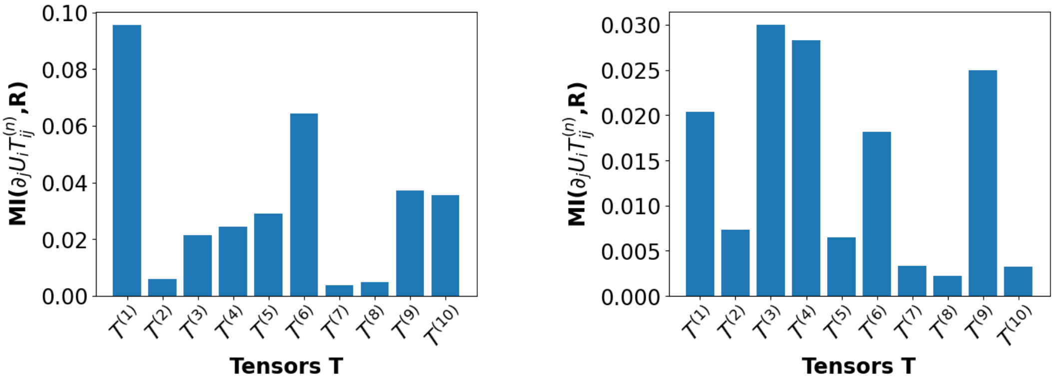

(a) Upstream Region

(b) Vortex Region

Figure 5.9: Mutual information between the t.k.e deficit and the basis tensors

As can be seen in Figure 5.9a, in the upstream region, mutual information is the highest between the second invariants of $T^{(1)}$ and $T^{(6)}$ basis tensors with MI>0.06. $T^{(3)}$, $T^{(4)}$ $T^{(5)}$,$T^{(9)}$, $T^{(10)}$ seem to have a weak but non negligible correlation. The author chose not to select $T^{(9)}$ and $T^{(10)}$ to keep the order of the models below 3. Finally $T^{(2)}$ does not seem to inform on R and is not selected.

In the region around the vortex, the mutual information between the tensors and R is different. The first thing that can be noted is that the mutual information is lower for all tensors. This is consistent with the fact that no informative model was found when using $R = 2kb^R_{ij}\partial_j U_i$. $T^{(3)}$ and $T^{(4)}$ are the tensors with the highest mutual information this time. It is followed by $T^{(9)}$, $T^{(1)}$ and $T^{(6)}$ with MI>0.015. Again $T^{(9)}$ is not selected to keep a model with a low order.

For b^Δ_{ij}, the mutual information between each components of the two tensors is plotted. The resulting mutual information can be seen in Figure 5.13. In the shear region, all tensors except for $T^{(10)}$ have a mutual information with b^Δ_{11} and b^Δ_{22} above 0.06. $T^{(1)}$ and $T^{(6)}$ have a medium to high mutual information with all components except for b^Δ_{13}. In the region close to the vortex, $T^{(1)}$ is the tensor whose components have the highest mutual information with the components of b^Δ_{ij}.

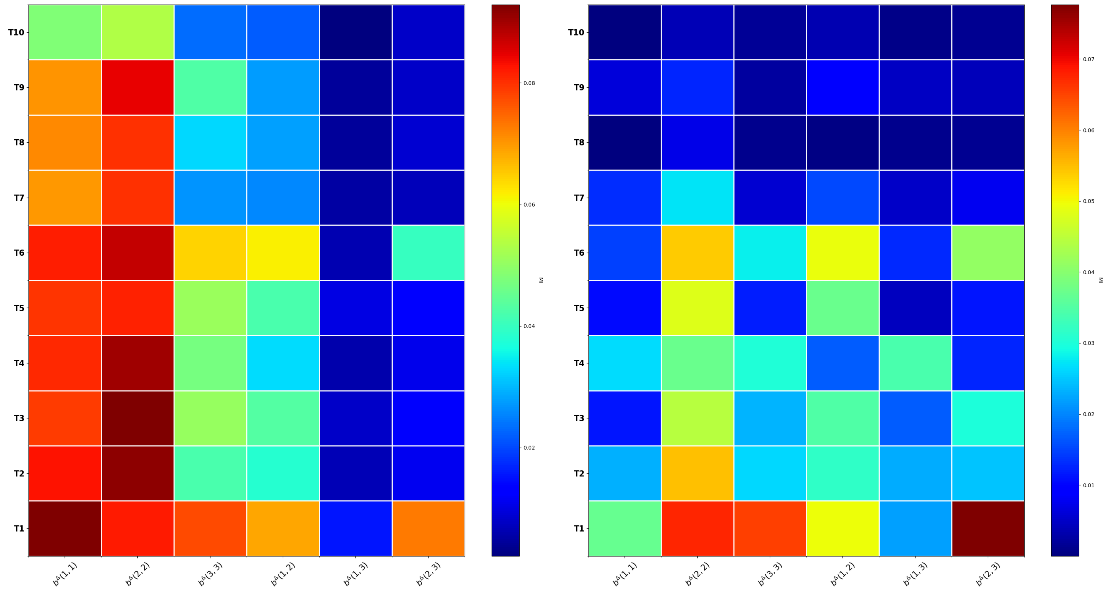

(a) Upstream Region

(b) Vortex Region

Figure 5.10: Mutual information between the b^Δ_{ij} and the basis tensors

The mutual information varies a lot depending on the components of b^Δ_{ij}. To choose the appropriate tensors, it was decided to also look at the mutual information between the tensors and P^Δ_k. In the upstream region, $T^{(1)}$ and $T^{(6)}$ have the highest mutual information and in the region where the vortex is present, they also show to be correlated with the data. $T^{(3)}$ and $T^{(4)}$ can also be considered to be important in this later region.

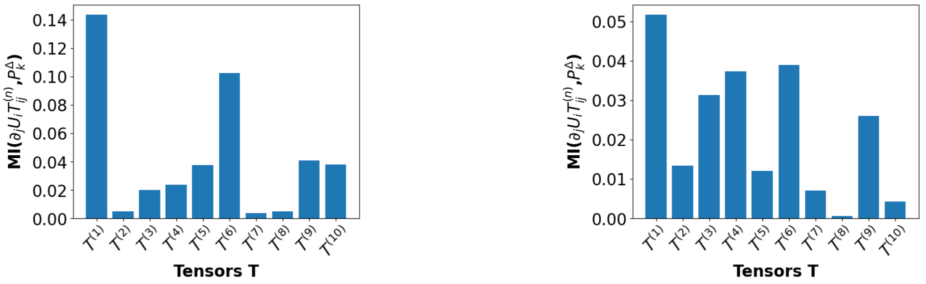

(a) Upstream Region

(b) Vortex Region

Figure 5.11: Mutual information between the P^Δ_k and the basis tensors

5.2.2. Invariants

The MI information between the invariants and the R and P_k^Δ is shown in Figure 5.12 and Figure 5.13. In the shear region, the mutual information between R and each invariant is almost the same. It is close to 0.06 and all invariants are kept as a consequence. In the vortex region, λ_1 dominates with a mutual information of 0.06.

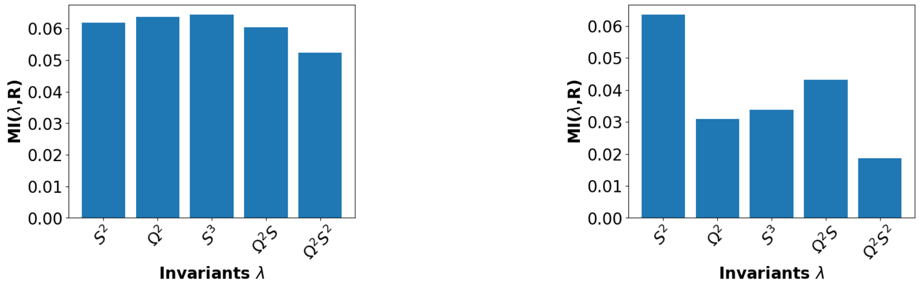

(a) Upstream Region (b) Vortex Region

Figure 5.12: Mutual information between the t.k.e deficit and the invariants

The mutual information between the invariants and P_k^Δ varies a lot depending on the region. This was expected as the vortex induces very different corrective fields compared to the upstream region. While all invariants seem to inform on P_k^Δ in the upstream region, in the vortex region λ_5 mutual information is reduced to 0.01.

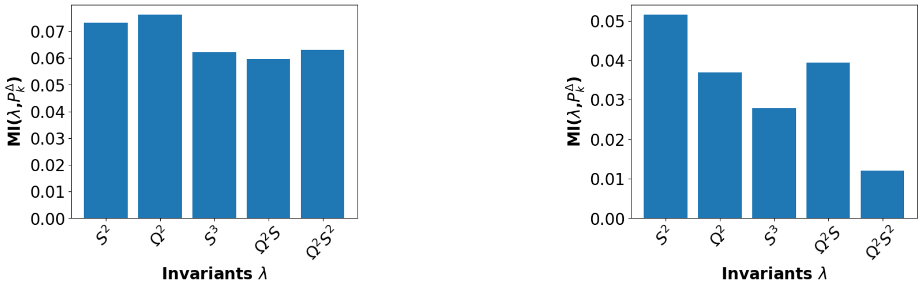

(a) Upstream Region (b) Vortex Region

Figure 5.13: Mutual information between the b_{ij}^Δ and the invariants

5.2.3. Physical features

The mutual information between the physical features and R and P_k^Δ is now studied. For R, the dominating features are the same in the two regions even if the mutual information is lesser in the vortex region. The Q criterion, turbulence intensity, wall distance based Reynolds number, viscosity ratio, vortex stretching and shear parameter have the highest mutual information. In addition, mutual information between the physical features and invariants was performed. The turbulence to mean strain time ratio is removed from the set due to its high mutual information with λ_1 in both the upstream region and the one close to the vortex. The self mutual information between features and invariants is shown in Appendix B.

Figure 5.15 shows the mutual information between the physical features and P_k^Δ. In the first region, the same physical features that had a high mutual information with R have a high mutual information with P_k^Δ. A notable addition is the ratio of pressure normal stresses to shear stresses. In the region close to the vortex , the Q criterion, the viscosity ratio and the ratio of pressure normal stresses to shear stresses have a mutual information above 0.06 and are being selected to be part of

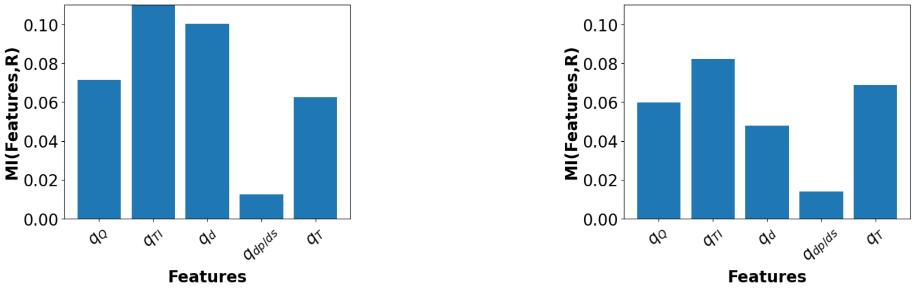

(a) Upstream Region (b) Vortex Region

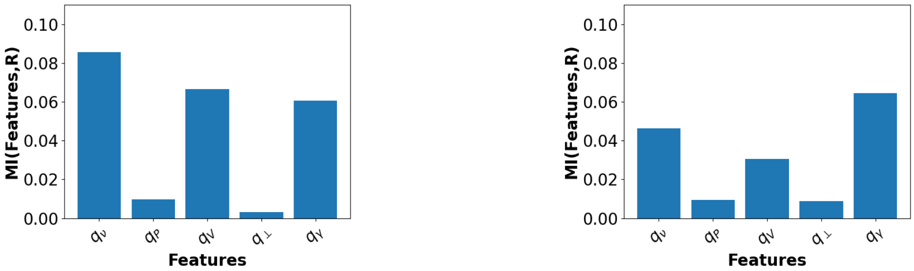

(c) Upstream Region (d) Vortex Region

Figure 5.14: Mutual information between the t.k.e deficit and the physical features

the library. The vortex stretching and shear parameter are also retained due to their performance in the first region.

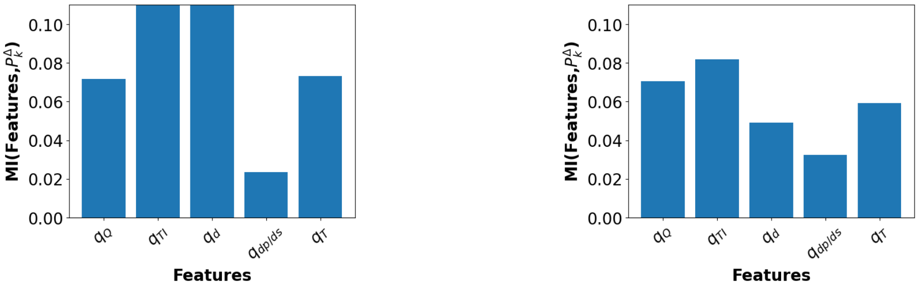

(a) Upstream Region (b) Vortex Region

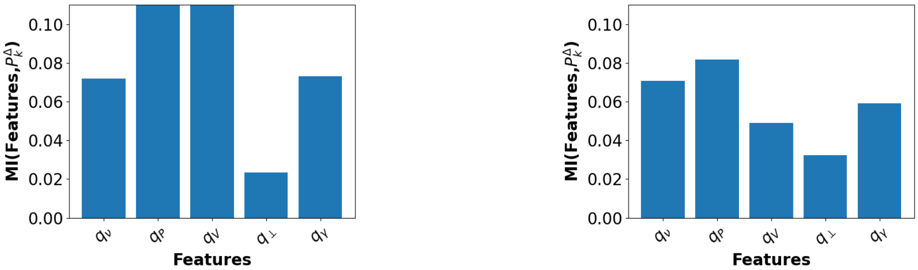

(c) UpstreamRegion (d) Vortex Region

Figure 5.15: Mutual information between the P_k^Δ and the physical features

In conclusion, the library can be build using the tensors and invariants specified in Table 5.1 for R and Table 5.2 for P_k^Δ. A function is retained if it has high mutual information with the target data in one of the two regions studied. The turbulence intensity q_{TI} has a high mutual information with R, but the author found unphysical spikes of R when using this feature and looking at profiles in the separation region before the vortex. This is due to the fact that the velocity is very close to zero while

Type	Description
Tensors	$T^{(1)}$,$T^{(6)}$,$T^{(3)}$, $T^{(4)}$
Invariants	λ_1,λ_2,λ_3,λ_4,λ_5
Physical features B_1^R	q_Q , q_d, q_v, q_V and q_γ

Table 5.1: Features Invariants and tensors for R selected from mutual information

the turbulent kinetic energy is non-zero in the boundary layer. Thus, the library retained for R does not include the turbulence intensity. For P_k^Δ, the turbulence intensity is also not retained because a similar behavior is expected.

Type	Description
Tensors	$T^{(1)}$,$T^{(6)}$,$T^{(3)}$, $T^{(4)}$
Invariants	λ_1,λ_2,λ_3,λ_4,λ_5
Physical features $B_1^{P_k^\Delta}$	q_Q , q_P, q_d, q_v, q_V and q_γ

Table 5.2: Features Invariants and tensors for P_k^Δ selected from mutual information

5.3. Model form for R and P_k^Δ

In order to validate the models obtained thanks to SpaRTA, the normalized error e is displayed and the models for R and P_k^Δ are compared to the true values of the corrective fields along different profiles. These profiles are located at different positions before the wing , in the main horseshoe vortex and on the side of the wing. Models found in the upstream region and the vortex region are evaluated on all profiles. As expected models trained upstream of the wing were not able to provide good models in the vortex region and only the models trained on the vortex region are shown here.

5.3.1. Model form for R

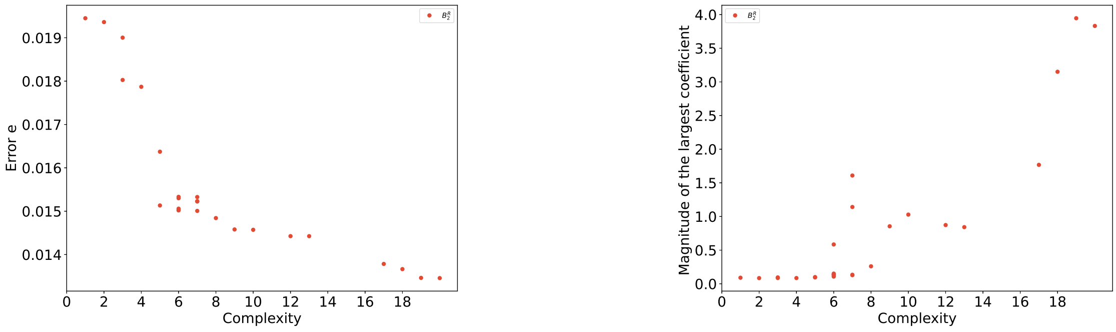

(a) Evolution of the error e with the complexity of the model for R

(b) Magnitude of the largest coefficient compared to the complexity of the model for R

Figure 5.16: Evolution of the error and coefficients with regards to complexity

In the vortex region, Figure 5.16a displays the evolution of the normalized root mean square error as defined in subsection 3.2.6 with the complexity of the model. It can be seen that the error decreases quickly up to a complexity of about 6. In this plot, the gain brought by more complex models does not seem to be significant. However, because R takes a broad range of values and in particular goes to extreme values in the region close to the wall, some further analysis is necessary to understand where each model is showing a good prediction of the true value of R .

Figure 5.16b displays the maximum value of the coefficients of a given model. Three categories of models can be distinguished here, models with very small coefficients that exist up until a complexity of 8, models with a maximum coefficient that is around 1 and then at higher complexity models with a largest coefficient above 3. Models with the smallest coefficients are likely to produce more stable simulations. In the following, models with coefficients below 1 are studied to evaluate if they provide a good representation of R.

Figure 5.17 displays some profiles of interest, all located in the second training region.
Profiles in Figure 5.17a are located upstream of the vortex in the symmetry plane. It can be seen that all models represented capture well the increase of R close to the wall. Small variations are smoothed out. At $X/T = -0.2092$, the models fail to predict the negative values around $Y/T = 0.01$ and most models remain positive on the full profile. Profiles in Figure 5.17b are located inside the vortex in the symmetry plane. Models $1577, 1580-1584$ seem to reproduce correctly the pattern of R, the increase of R is correctly located although a bit small at $X/T = -0.1301$. In the full region, the error e is roughly the same for models $1580-1584$ and is higher for model 1577.

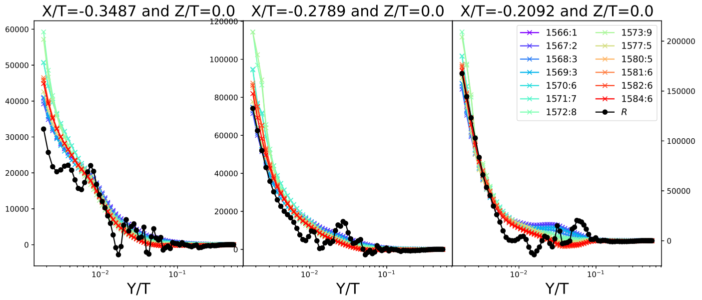

(a) Profiles in the separation region before the vortex

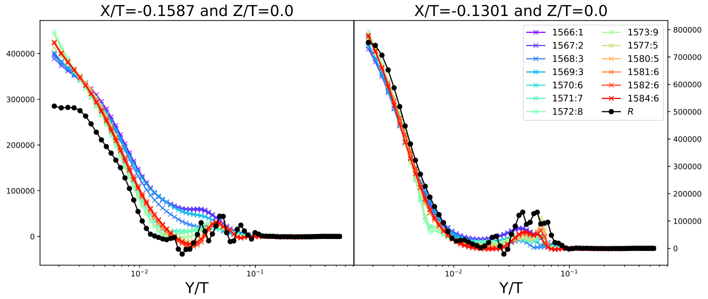

(b) Profiles in the vortex

Figure 5.17: Predictions of R versus the true values with training in the second region

In Figure 5.17 , the performance of the models was tested in the region of their training. However, in the absence of a classifier for different regions, the models will be applied to the full domain. The predictive power of the models upstream of the wing, outside of their training region is shown in Figure 5.18. Overall, all models predict correctly the increase in R around $Y/T = 4.10^{-3}$ but they fail to return to lower values before re-increasing closer to the wall as was shown in Figure 5.5 . This is maybe due to the limit imposed on $y+$ that prevents the models to learn the proper behavior for $y+ < 10$.

Based on the previous discussion, five models are selected to represent best the turbulent kinetic energy deficit. They can be separated into two groups: one with complexity 5 and one with complexity 6.

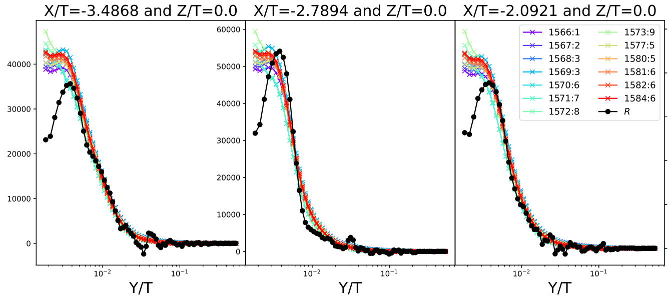

Figure 5.18: Comparison of models trained in the vortex region on profiles upstream of it

The models with complexity 5 are:

$$M_R^{(1577)} = 2k\partial_j U_i T^{(1)}(-0.9571 q_\nu) + \omega k(0.0947 + 0.0627 q_Q q_\nu^{0.5} - 0.0017 q_\gamma^{0.5} - 0.0462 q_\nu^{1.5}) \tag{5.1}$$

$$M_R^{(1580)} = 2k\partial_j U_i T^{(1)}(-0.3860 q_\nu^{0.5}) + \omega k(0.09945 + 0.0992 q_Q q_d^{0.5} \lambda_1^{0.5} - 0.0815 q_\nu + 0.0287 q_V^{1.5}) \tag{5.2}$$

And the models with complexity 6 are:

$$M_R^{(1581)} = 2k\partial_j U_i T^{(1)}(-0.2910 q_\nu^{0.5}) + \omega k(0.0979 + 0.1070 q_Q q_d^{0.5} \lambda_1^{0.5} + -0.0861 q_\nu + 0.0357 q_V - 0.0077 q_V^{1.5}) \tag{5.3}$$

$$M_R^{(1582)} = 2k\partial_j U_i T^{(1)}(-0.2503 q_\nu^{0.5}) + \omega k(0.0995 + 0.1510 q_Q q_d^{0.5} \lambda_1^{0.5} - 0.03417 q_Q q_\nu^{0.5} - 0.0892 q_\nu + 0.0371 q_V^{1.5}) \tag{5.4}$$

$$M_R^{(1584)} = 2k\partial_j U_i T^{(1)}(0.5840 q_\nu - 0.9214 q_\nu^{0.5}) + \omega k(0.1001 + 0.1278 q_Q q_d^{0.5} \lambda_1^{0.5} - 0.01417 q_Q q_\nu^{0.5} - 0.0771 q_\nu) \tag{5.5}$$

By comparing these five models to the non-selected ones, one can make the following remarks:

- $\omega k * 0.09$, which is the model of complexity 1, is used by most models to reproduce the increase of R close to the wall.
- The introduction of the normalized Q criterion in the selected models improves the behavior close to the vortex compared to the models with lower complexity. However, models with higher complexity do not necessarily use this feature but also use the vortex stretching feature.
- The models selected here, based on their reasonable complexity, are very similar showing some combinations of the Q criterion, the viscosity ratio and the wall distance based Reynolds number.
- Additional terms are based on the shear parameter and the vortex stretching.

5.3.2. Model form for P_k^Δ

Due to the difficulty of finding models for b_{ij}^Δ, it was decided to find models for P_k^Δ. Although no good models were found for P_k^Δ , the comparison between the true values and the models is displayed for a few profiles in Figure 5.19 to understand in which way the modeling fails. The previous constraints on complexity and magnitude of the maximum coefficient are relaxed and the maximum complexity displayed is chosen to be 10 with coefficients lesser than 5. It can be seen in Figure 5.19a that the performance of the found models, initially good upstream of the wing is getting worst when approaching the vortex. This is coherent with the observation that the shape of P_k^Δ is very simple upstream. The prediction and true values are almost in opposition at $X/T = -0.2092$.

The profiles in the vortex shown in Figure 5.19b are slightly better as they capture the negative peak at $Y/T = 0.04$. However, the positive production of turbulent kinetic energy closer to the wall is completely mispredicted by all models. In conclusion, the two positive and negative lumps that are lifted when going upstream are not being captured by SpaRTA.

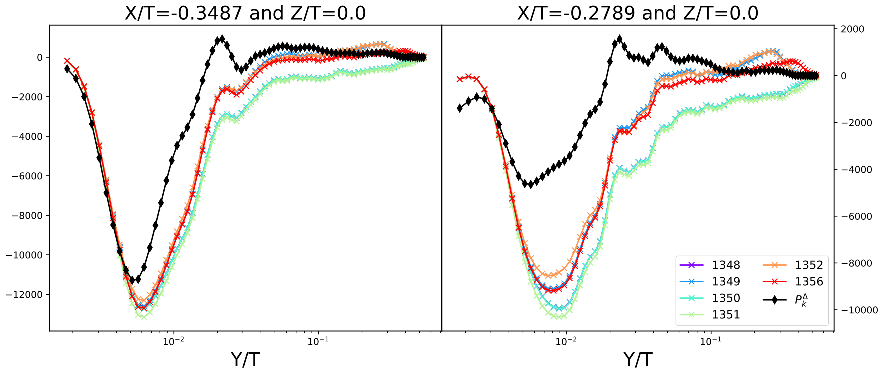

(a) Profiles in the region with separation before the vortex

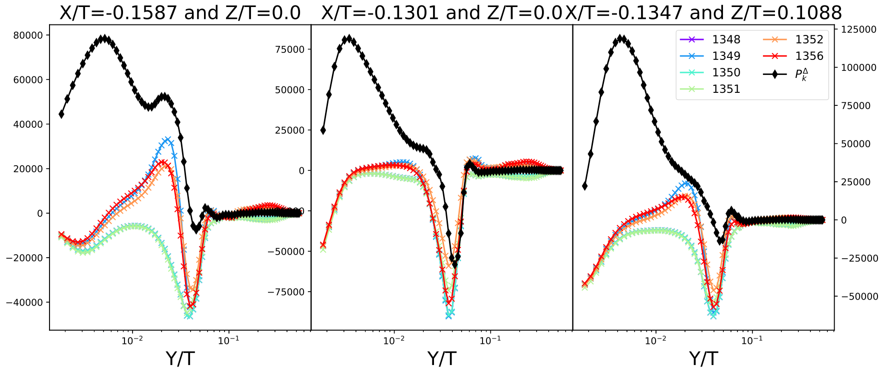

(b) Profiles in the vortex

Figure 5.19: Predictions of P_k^Δ versus the true values in the vortex region

Out of the models displayed in Figure 5.19, the models with the lowest error e are:

$$M^{1349}_{P_k^\Delta} = -2k\partial_j U_i (0.7202T^{(1)} - 4.5743q_v^{0.5}T^{(1)}) \tag{5.6}$$

$$M^{1352}_{P_k^\Delta} = -2k\partial_j U_i (0.7294T^{(1)} - 4.2071T^{(4)} - 3.4781q_v^{0.5}T^{(1)}) \tag{5.7}$$

$$M^{1356}_{P_k^\Delta} = -2k\partial_j U_i (-1.91778q_d^{0.5}T^{(1)} + 0.2258q_d T^{(1)} + 0.7062T^{(1)} + 0.8253T^{(6)} + 0.2687\lambda_1^{0.5}T^{(1)}) \tag{5.8}$$

The expressions of the models reveal that all of them rely on $T^{(1)}$. This is probably because outside of the area in the immediate vicinity with the vortices, the Boussinesq approximation remains valid and it can also be linked to the shape of P_k^Δ in Figure 5.5 . The other tensors used are $T^{(4)}$ and $T^{(6)}$. The models within the range of coefficients and complexity chosen only use q_v and q_d for the physical features. This is surprising as other physical features had comparable mutual information with P_k^Δ but are not used in the models.
Given the inability of the models found in this study to reproduce the key characteristics of P_k^Δ in the vortex region, it was decided by the author not to implement these models in OpenFoam.

6

Conclusions and Recommendations

Junction flows are encountered in hydrodynamics, aerospace and many other industrial domains. The adverse pressure gradient caused by the presence of the obstacle in the flow leads to the separation of the boundary layer and to a system of unsteady horseshoe vortices in turbulent flows. In aerospace, the body wing junction flow is increasing the total drag of the airplane due to the presence of interference drag. Aerodynamic shape optimization has been used to find a new design for the junction that aims at reducing its drag. Previous studies of this Anti-Fairing design used RANS simulations or wall-modeled LES due to their reduced computational cost. However, these methods have proved to be inaccurate in predicting some major features of junction flows such as the location, strength and shape of the main horseshoe vortex. Based on the gaps found in the existing literature the objective of this study was :

To produce a wall resolved LES of the Anti-Fairing body wing junction and to enhance the accuracy of RANS turbulence models in the case of body wing junction flows using a data-driven turbulence modeling approach (namely SpaRTA)

The conclusions and recommendations for future work are presented in this chapter.

6.1. Conclusions

A wall resolved LES for the Anti-Fairing design was performed in this study. This specific configuration also leads to the creation of a system of unsteady vortices. The bimodal behavior that characterizes the switching between a zero flow mode and a backflow mode was observed as well as the specific C-shape of the time-averaged main horseshoe vortex. The comparison was made with the wall resolved LES of Alberts [2]. The presence of the Anti-Fairing results in different modifications of the flow compared to the baseline case. Streamlines on the bottom wall upstream of the wing reveal that separation is delayed in the case of the Anti-Fairing and profiles of velocity show that the size of the separation is smaller than the one of the baseline case. The visualizations of the vorticity in the vicinity of the wing show that the Anti-Fairing causes the vortex to be located closer to the wall but does not change significantly the distance to the wing. The turbulent kinetic energy in the symmetry plane is reduced compared to the baseline case which could be explained by the convex nature of the dent. Along the wing, the vortex is mostly following the shape of the wing. In the case of the Anti-Fairing the distance between the two legs of the vortex is more important than in the baseline case, this is especially visible in the wake of the wing for the velocity plots. This is in agreement with the experiment of Belligoli et al. [6]. The location of the vortex closer to the wall, the weaker separation and the distance between the legs of the main horseshoe vortex are in agreement with the hypothesis of Belligoli et al. [6] of the higher Momentum Deficit Factor in the case of the Anti-Fairing.

Using the wall resolved data, the data-driven algorithm SpARTA was used to generate algebraic models for correction to the RANS turbulence models. The RANS model to be corrected is the $k-\omega$ SST model. The k-corrective frozen approach was successfully used to generate two correction fields: one being a turbulent kinetic energy deficit and the other a correction to the Reynolds stress anisotropy. The analysis of these two fields reveals two main regions of corrections : one in the upstream boundary layer and the other in the vicinity of the vortices. The corrections in the vortex regions have very big variations in a small area. Looking downstream the correction magnitude decreases. When adding the frozen corrections to the turbulent kinetic energy and the Reynolds stress in a $k-\omega$ SST simulation, one can see the very good match between the corrected RANS fields and the LES. The shape, magnitude and location of the main horseshoe vortex are properly captured. Adding only the corrections to the turbulent kinetic energy and the producing term resulting from the correction to the anisotropy results in a small improvement over the baseline RANS model. Mutual information was then used to determine relevant tensors, features and invariants to use in the models for the two corrective terms. Finally, models for the turbulent kinetic energy and the P_k^{Δ} were obtained with the SpaRTA algorithm. The found models have a good performance outside the vortex region but some important discrepancies can be observed between the true fields and their models in the vortex region. For the turbulent kinetic energy, the negative values are often not properly captured and for P_k^{Δ}, the models are really failing to capture the positive/negative shift of the correction in this region.
Using the SpaRTA methodology to obtain good models for body wing junction is likely to require more steps and constraints than the ones used in the time of this study.

6.2. Recommendations

Following the work done during this thesis, some recommendations can be made for future research:

- Using the two wall resolved LES, the drag could be investigated to provide a definite answer on the capacity of the Anti-Fairing to reduce drag in the junction.
- Additional constraints, features or invariants could be investigated to enhance the performance of SpaRTA for body wing junction flows.
- Alternatively, other data-driven techniques could be tested on this case.
- As the mean features of junction flows are the results of the dynamics of the horseshoe system, it would be interesting to test data driven-techniques for unsteady but low-cost simulations such as URANS simulations.

A

Appendix A

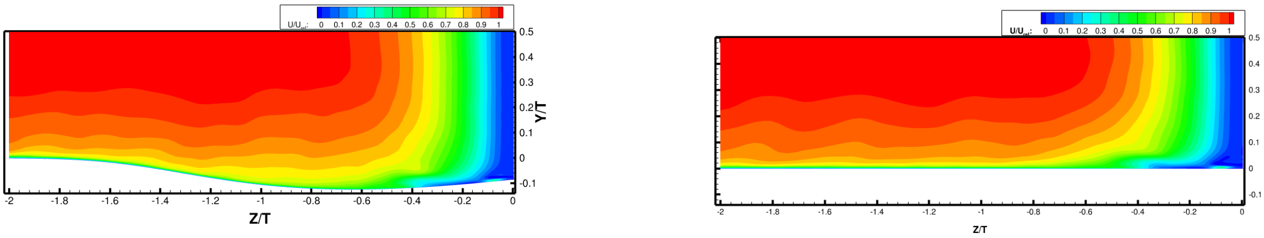

(a) Anti-Fairing at $X/T = 0$ - Present study

(b) Baseline case at $X/T = 0$ from Alberts [2]

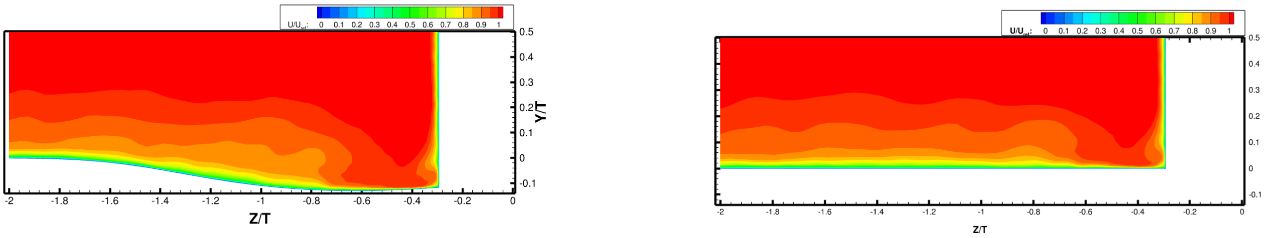

(c) Anti-Fairing at $X/T = 2.8$ - Present study

(d) Baseline case at $X/T = 2.8$ from Alberts [2]

Figure A.1: Streamwise velocity

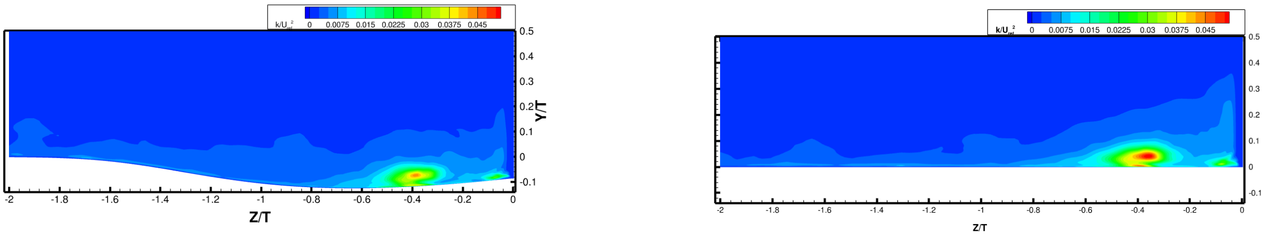

(a) Anti-Fairing at $X/T = 0$ - Present study

(b) Baseline case at $X/T = 0$ from Alberts [2]

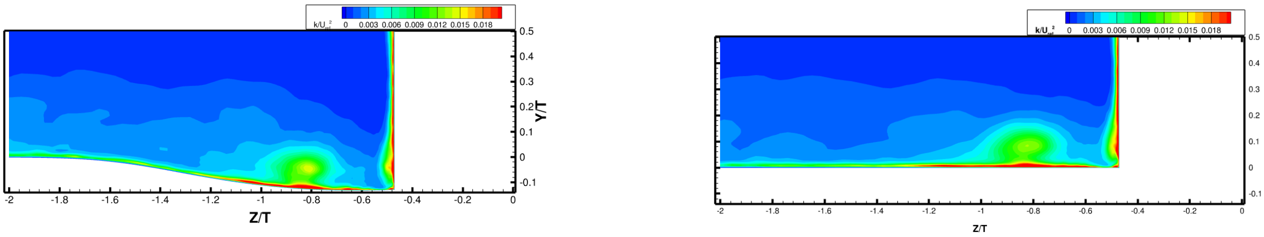

(c) Anti-Fairing at $X/T = 1.4$ - Present study

(d) Baseline case at $X/T = 1.4$ from Alberts [2]

Figure A.2: Turbulent kinetic energy

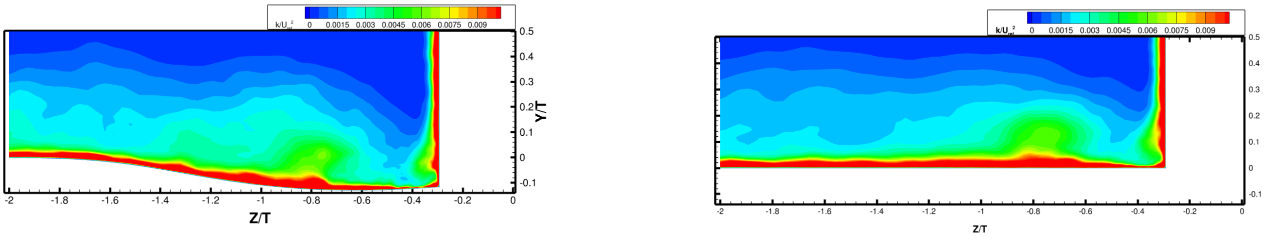

(a) Anti-Fairing at $X/T = 2.8$ - Present study

(b) Baseline case at $X/T = 2.8$ from Alberts [2]

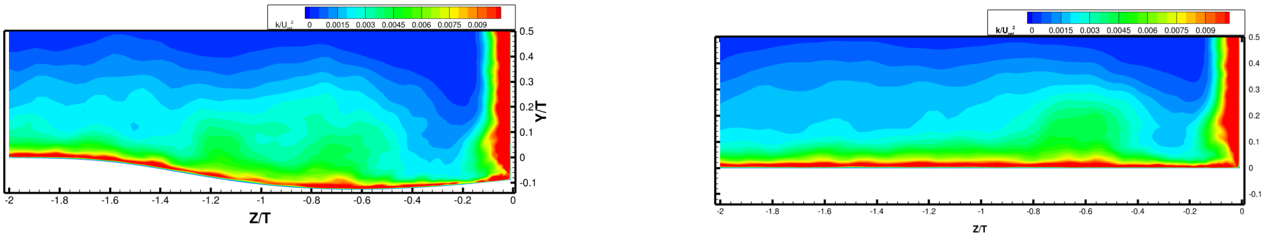

(c) Anti-Fairing at $X/T = 4.2$ - Present study

(d) Baseline case at $X/T = 4.2$ from Alberts [2]

Figure A.3: Turbulent kinetic energy

B

Appendix B

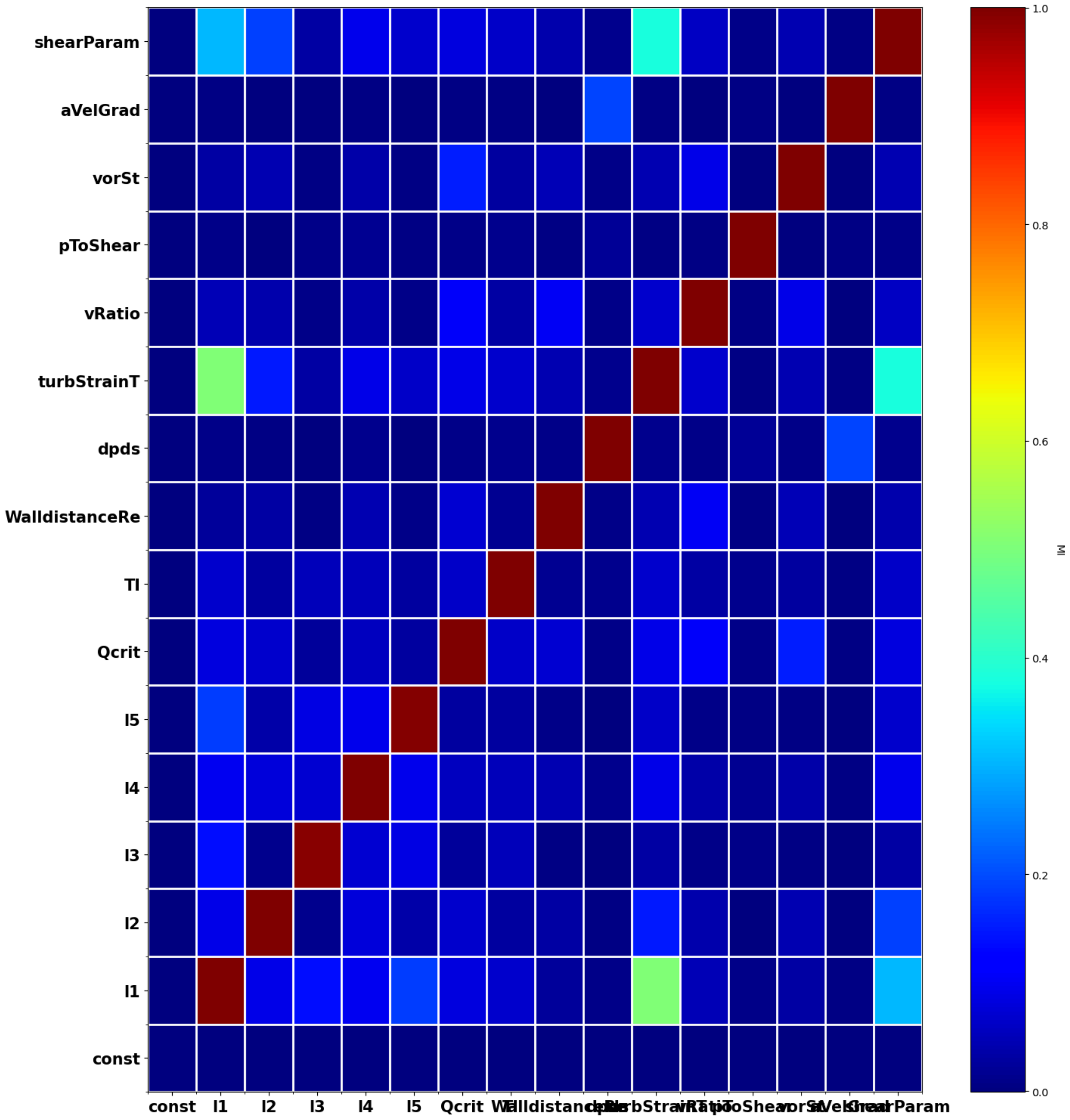

Figure B.1: Self mutual information between invariants and physical features in the vortex region

Bibliography

[1] Anwar Ahmed and Javed Khan. *Effect of sweep on wing-body juncture flow*. AIAA-95-0868, 1995. doi: 10.2514/6.1995-868. URL `https://arc.aiaa.org/doi/abs/10.2514/6.1995-868`.

[2] Jasper Alberts. Les of a novel wing/body junction : Anti-fairing. Master's thesis, TU Delft, 2021.

[3] D. D. Apsley and M. A. Leschziner. Investigation of advanced turbulence models for the flow in a generic wing-body junction. *Flow, Turbulence and Combustion*, 67(1):25–55, 2001. doi: 10.1023/A:1013598401276.

[4] T. J. Barber. An investigation of strut-wall intersection losses. *Journal of Aircraft*, 15(10):676–681, 1978. doi: 10.2514/3.58427. URL `https://doi.org/10.2514/3.58427`.

[5] D Barberis, P Molton, and T Malaterre. Control of 3d turbulent boundary layer separation caused by a wing–body junction. *Experimental Thermal and Fluid Science*, 16(1):54–63, 1998. ISSN 0894-1777. doi: https://doi.org/10.1016/S0894-1777(97)10012-7. URL `https://www.sciencedirect.com/science/article/pii/S0894177797100127`.

[6] Z. Belligoli, A. J. Koers, R. P. Dwight, and G. Eitelberg. Using an anti-fairing to reduce drag at wing/body junctions. *AIAA Journal*, 57(4):1468–1480, 2019. doi: 10.2514/1.J057481.

[7] Steven L. Brunton, Bernd R. Noack, and Petros Koumoutsakos. Machine learning for fluid mechanics. *Annual Review of Fluid Mechanics*, 52(1):477–508, 2020. doi: 10.1146/annurev-fluid-010719-060214. URL `https://doi.org/10.1146/annurev-fluid-010719-060214`.

[8] W. J. Devenport, N. K. Agarwal, M. B. Dewitz, R. L. Simpson, and K. Poddar. Effects of a fillet on the flow past a wing-body junction. *AIAA Journal*, 28(12):2017–2024, 1990. doi: 10.2514/3.10517. URL `https://doi.org/10.2514/3.10517`.

[9] William J. Devenport and Roger L. Simpson. Time-dependent and time-averaged turbulence structure near the nose of a wing-body junction. *Journal of Fluid Mechanics*, 210:23–55, 1990. doi: 10.1017/S0022112090001215.

[10] William J. Devenport, Roger L. Simpson, Michael B. Dewitz, and Naval K. Agarwal. Effects of a leading-edge fillet on the flow past an appendage-body junction. *AIAA Journal*, 30(9):2177–2183, 1992. doi: 10.2514/3.11201. URL `https://doi.org/10.2514/3.11201`.

[11] Karthik Duraisamy. Perspectives on machine learning-augmented reynolds-averaged and large eddy simulation models of turbulence. *Phys. Rev. Fluids*, 6:050504, May 2021. doi: 10.1103/PhysRevFluids.6.050504. URL `https://link.aps.org/doi/10.1103/PhysRevFluids.6.050504`.

[12] Karthik Duraisamy, Gianluca Iaccarino, and Heng Xiao. Turbulence modeling in the age of data. *Annual Review of Fluid Mechanics*, 51(1):357–377, 2019. doi: 10.1146/annurev-fluid-010518-040547. URL `https://doi.org/10.1146/annurev-fluid-010518-040547`.

[13] J. Fleming, R. Simpson, and W. Devenport. An experimental study of a turbulent wing-body junction and wake flow. Technical Report Technical Report No. VPI-AOE-179, Aerospace and Ocean Engineering Departement, Virginia Polytechnic Institute and State University, 1991.

[14] J. L. Fleming, R. L. Simpson, J. E. Cowling, and W. J. Devenport. An experimental study of a turbulent wing-body junction and wake flow. *Experiments in Fluids : Experimental Methods and their Applications to Fluid Flow*, 14(5):366–378, 1993. doi: 10.1007/BF00189496.

[15] Fabien Gand, Sebastien Deck, Vincent Brunet, and Pierre Sagaut. Flow dynamics past a simplified wing body junction. *Physics of Fluids*, 22(11):115111, 2010. doi: 10.1063/1.3500697.

[16] Michel Goderie. Enhancement of data-driven turbulence models for wind turbine wake applications. Master's thesis, TU Delft, 2020.

[17] Jasper P. Huijing, Richard P. Dwight, and Martin Schmelzer. Data-driven rans closures for three-dimensional flows around bluff bodies. *Computers and Fluids*, 225:104997, 2021. ISSN 0045-7930. doi: https://doi.org/10.1016/j.compfluid.2021.104997. URL `https://www.sciencedirect.com/science/article/pii/S0045793021001638`.

[18] D. A. Jones and D. Clarke. Simulation of a wing-body junction experiment using the fluent code. 2005.

[19] Mikael L.A. Kaandorp and Richard P. Dwight. Data-driven modelling of the reynolds stress tensor using random forests with invariance. *Computers & Fluids*, 202:104497, 2020. ISSN 0045-7930. doi: https://doi.org/10.1016/j.compfluid.2020.104497. URL `https://www.sciencedirect.com/science/article/pii/S0045793020300700`.

[20] Michael A. Kegerise, Dan Neuhart, Judith Hannon, and Christopher L. Rumsey. An experimental investigation of a wing-fuselage junction model in the nasa langley 14- by 22-foot subsonic wind tunnel. 2022/02/09 2019. doi: doi:10.2514/6.2019-0077. URL `https://doi.org/10.2514/6.2019-0077`.

[21] S.A. Kim, D.A. Walker, and Simpson R.L. Observation and measurements of flow structures in the stagnation region of a wing- body junction, 1991.

[22] Alexander Kraskov, Harald Stögbauer, and Peter Grassberger. Estimating mutual information. *Phys. Rev. E*, 69:066138, Jun 2004. doi: 10.1103/PhysRevE.69.066138. URL `https://link.aps.org/doi/10.1103/PhysRevE.69.066138`.

[23] Sampath Kumar. Wall-resolved large eddy simulation of a wing-body junction: High-fidelity data generation for data-driven turbulence modelling. Master's thesis, TU Delft, 2019.

[24] J. P. Lee, J. Chen, and C. Hsin. Study of junction flow structures with different turbulence models. *Journal of Marine Science and Technology (Taiwan)*, 25(2):178–185, 2017. URL `10.6119/JMST-016-1116-2`.

[25] J. Ling and J. Templeton. Evaluation of machine learning algorithms for prediction of regions of high reynolds averaged navier stokes uncertainty. *Physics of Fluids*, 27(8):085103, 2015. doi: 10.1063/1.4927765. URL `https://aip.scitation.org/doi/abs/10.1063/1.4927765`.

[26] Julia Ling, Reese Jones, and Jeremy Templeton. Machine learning strategies for systems with invariance properties. *Journal of Computational Physics*, 318:22–35, 2016. ISSN 0021-9991. doi: https://doi.org/10.1016/j.jcp.2016.05.003. URL `https://www.sciencedirect.com/science/article/pii/S0021999116301309`.

[27] Julia Ling, Andrew Kurzawski, and Jeremy Templeton. Reynolds averaged turbulence modelling using deep neural networks with embedded invariance. *Journal of Fluid Mechanics*, 807: 155–166, 2016. doi: 10.1017/jfm.2016.615.

[28] F. R. Menter. Two-equation eddy-viscosity turbulence models for engineering applications. *AIAA Journal*, 32(8):1598–1605, 1994. doi: 10.2514/3.12149. URL `https://doi.org/10.2514/3.12149`.

[29] K. C. Muck, P. H. Hoffmann, and P. Bradshaw. The effect of convex surface curvature on turbulent boundary layers. 161:347–369, 1985. doi: DOI: 10.1017/S002211208500297X. URL `https://www.cambridge.org/core/article/effect-of-convex-surface-curvature-on-turbulent-boundary-layers/7D7B5D4067AF8B8B8527E342446EDEFB`.

[30] Timofey Mukha and Mattias Liefvendahl. Eddylicious: A python package for turbulent inflow generation. *SoftwareX*, 7:112–114, 2018. ISSN 2352-7110. doi: https://doi.org/10.1016/j.softx.2018.04.001. URL `https://www.sciencedirect.com/science/article/pii/S2352711018300487`.

[31] Franck Nicoud and Frédéric Ducros. Subgrid-scale stress modelling based on the square of the velocity gradient tensor. *Flow Turbulence and Combustion*, 62:183–200, 09 1999. doi: 10.1023/A:1009995426001.

[32] R. Paciorri, A. Bonfiglioli, A. Di Mascio, and B. Favini. Rans simulations of a junction flow. *International Journal of Computational Fluid Dynamics*, 19(2):179–189, 2005. doi: 10.1080/10618560410001729126.

[33] Joongcheol Paik, Cristian Escauriaza, and Fotis Sotiropoulos. On the bimodal dynamics of the turbulent horseshoe vortex system in a wing-body junction. *Physics of Fluids*, 19(4):045107, 2007. doi: 10.1063/1.2716813.

[34] Eric J. Parish and Karthik Duraisamy. A paradigm for data-driven predictive modeling using field inversion and machine learning. *Journal of Computational Physics*, 305:758–774, 2016. ISSN 0021-9991. doi: https://doi.org/10.1016/j.jcp.2015.11.012. URL `https://www.sciencedirect.com/science/article/pii/S0021999115007524`.

[35] D. B. Philips, J. M. Cimbala, and A. L. Treaster. Suppression of the wing-body junction vortex by body surface suction. *Journal of Aircraft*, 29(1):118–122, 1992. doi: 10.2514/3.46134. URL `https://doi.org/10.2514/3.46134`.

[36] S. B. Pope. A more general effective-viscosity hypothesis. *Journal of Fluid Mechanics*, 72(2): 331–340, 1975. doi: 10.1017/S0022112075003382.

[37] S. Ryu, M. Emory, G. Iaccarino, A. Campos, and K. Duraisamy. Large-eddy simulation of a wing-body junction flow. *AIAA Journal*, 54(3):793–804, 2016. doi: 10.2514/1.J054212.

[38] Martin Schmelzer, Richard P. Dwight, and Paola Cinnella. Discovery of algebraic reynolds-stress models using sparse symbolic regression. *Flow, Turbulence and Combustion*, 104 (2):579–603, 2020. doi: 10.1007/s10494-019-00089-x. URL `https://doi.org/10.1007/s10494-019-00089-x`.

[39] Peter J. Schmid. Dynamic mode decomposition of numerical and experimental data. *Journal of Fluid Mechanics*, 656:5–28, 2010. doi: 10.1017/S0022112010001217.

[40] Takaaki Shizawa, Shinji Honami, and Masahiko Yamamoto. *Experimental study of horseshoe vortex at wing/body junction with attack angle by triple hot-wire.* AIAA-96-0323, 1996. doi: 10.2514/6.1996-323. URL `https://arc.aiaa.org/doi/abs/10.2514/6.1996-323`.

[41] R. L. Simpson. Junction flows. *Annual Review of Fluid Mechanics*, 33:415–443, 2001. doi: 10.1146/annurev.fluid.33.1.415.

[42] Anand Pratap Singh, Shivaji Medida, and Karthik Duraisamy. Machine-learning-augmented predictive modeling of turbulent separated flows over airfoils. *AIAA Journal*, 55(7):2215–2227, 2017. doi: 10.2514/1.J055595. URL `https://doi.org/10.2514/1.J055595`.

[43] Joseph Smagorinsky. General circulation experiments with the primitive equations : I. the basic experiment. *Monthly Weather Review*, 91(3):99 – 164, 1963. doi: 10.1175/1520-0493(1963)091<0099:GCEWTP>2.3.CO;2. URL `https://journals.ametsoc.org/view/journals/mwre/91/3/1520-0493_1963_091_0099_gcewtp_2_3_co_2.xml`.

[44] Julia Steiner, Richard Dwight, and Axelle Viré. Data-driven turbulence modeling for wind turbine wakes under neutral conditions. *Journal of Physics: Conference Series*, 1618:062051, sep 2020. doi: 10.1088/1742-6596/1618/6/062051. URL `https://doi.org/10.1088/1742-6596/1618/6/062051`.

[45] Jian-Xun Wang, Jin-Long Wu, and Heng Xiao. Physics-informed machine learning approach for reconstructing reynolds stress modeling discrepancies based on dns data. *Phys. Rev. Fluids*, 2:034603, Mar 2017. doi: 10.1103/PhysRevFluids.2.034603. URL `https://link.aps.org/doi/10.1103/PhysRevFluids.2.034603`.

[46] Jack Weatheritt and Richard Sandberg. A novel evolutionary algorithm applied to algebraic modifications of the rans stress–strain relationship. *Journal of Computational Physics*, 325:22–37, 2016. ISSN 0021-9991. doi: https://doi.org/10.1016/j.jcp.2016.08.015. URL `https://www.sciencedirect.com/science/article/pii/S0021999116303643`.

[47] Jinlong Wu, Heng Xiao, and Eric Paterson. Physics-informed machine learning approach for augmenting turbulence models: A comprehensive framework. *Physical Review Fluids*, 2018.

[48] Yaomin Zhao, Harshal D. Akolekar, Jack Weatheritt, Vittorio Michelassi, and Richard D. Sandberg. Rans turbulence model development using cfd-driven machine learning. *Journal of Computational Physics*, 411:109413, 2020. ISSN 0021-9991. doi: https://doi.org/10.1016/j.jcp.2020.109413. URL `https://www.sciencedirect.com/science/article/pii/S002199912030187X`.

[49] Semİh M. Ölçmen and Roger L. Simpson. An experimental study of a three-dimensional pressure-driven turbulent boundary layer. *Journal of Fluid Mechanics*, 290:225–262, 1995. doi: 10.1017/S0022112095002497.